

The Chemical Composition of Extreme-Velocity Stars*†

HENRIQUE REGGIANI,¹ ALEXANDER P. JI,² KEVIN C. SCHLAUFMAN,³ ANNA FREBEL,⁴ LINA NECIB,⁴ TYLER NELSON,⁵
KEITH HAWKINS,⁵ AND JHON YANA GALARZA⁶

¹*The Observatories of the Carnegie Institution for Science, 813 Santa Barbara St., Pasadena, CA 91101, USA*

²*Department of Astronomy and Astrophysics, University of Chicago, Chicago IL 60637, USA*

³*William H. Miller III Department of Physics and Astronomy, Johns Hopkins University, 3400 N Charles St, Baltimore, MD 21218, USA*

⁴*Massachusetts Institute of Technology, Cambridge, MA, USA*

⁵*Department of Astronomy, The University of Texas at Austin, 2515 Speedway Boulevard, Austin, TX 78712, USA*

⁶*CRAAM, Mackenzie Presbyterian University, Rua da Consolação, 896, São Paulo, Brazil*

(Received February 24, 2022)

Submitted to AAS Journals

ABSTRACT

Little is known about the origin of the fastest stars in the Galaxy. Our understanding of the Milky Way and surrounding dwarf galaxies chemical evolution history allows us to use the chemical composition of a star to investigate its origin, and say whether a star was formed in-situ or was accreted. However, the fastest stars, the hypervelocity stars, are young and massive and their chemical composition has not yet been analyzed. Though it is difficult to analyze the chemical composition of a massive young star, we are well versed in the analysis of late-type stars. We have used high-resolution ARCES/3.5m Apache Point Observatory, MIKE/Magellan spectra to study the chemical details of 15 late-type hypervelocity stars candidates. With Gaia EDR3 astrometry and spectroscopically determined radial velocities we found total velocities with a range of 274 - 520 km s⁻¹ and mean value of 381 km s⁻¹. Therefore, our sample stars are not fast enough to be classified as Hypervelocity stars, and are what is known as extreme-velocity stars. Our sample has a wide iron abundance range of $-2.5 \leq [\text{Fe}/\text{H}] \leq -0.9$. Their chemistry indicate that at least 50% of them are accreted extragalactic stars, with iron-peak elements consistent with prior sub-Chandrasekhar mass type Ia supernova enrichment. Without indication of binary companions, their chemical abundances and orbital parameters are indicative that they are the accelerated tidal debris of disrupted dwarf galaxies.

Keywords: Hypervelocity stars (776); Population II stars (1284); Stellar abundances (1577); Stellar populations(1622)

1. INTRODUCTION

The existence of Hypervelocity stars (HVSs) was first proposed by Hills (1988). Hills (1988) coined the term Hypervelocity stars to describe stars ejected with total velocities exceeding 1000 km s⁻¹ after a stellar en-

counter with a massive black hole. Hills theorized that an interaction of a pair of binary stars with the supermassive black hole Sagittarius A could result in the ejection of one of the stars at such velocities. The proposed acceleration mechanism is known as the Hills mechanism. Finding a HVS coming from the Galactic center, argued Hills, would be definitive evidence of the presence of a massive black hole in the Galactic center. Hills continued his theoretical study of these objects in Hills (1991, 1992), but it took almost 20 years for a HVS to be found. Brown et al. (2005) reported the discovery of SDSS J090745.0+024507, a 853 km s⁻¹ star found to be unbound from the Galactic potential. To explain such

Corresponding author: Henrique Reggiani
hreggiani@carnegiescience.edu

* This paper includes data gathered with the 6.5-meter Magellan Telescopes located at Las Campanas Observatory, Chile.

† This paper includes data gathered with the 3.5-meter Telescope at Apache Point Observatory.

a speed, a dynamical interaction with a compact object is needed (Brown 2015).

Since the discovery of SDSS J090745.0+024507 the interest in HVSs has considerably increased, both from theoretical and observational perspectives. Theorists have put forward different ways to explain how stars can be accelerated to high velocities: a variation of the Hills mechanism via three-body interactions (Yu & Tremaine 2003); ejection of the companion when one star in a binary system explodes as a supernova (Blaauw 1961); tidal debris from a dwarf galaxy recently disrupted near the center of the Milky Way (Abadi et al. 2009); dynamical ejection from dense stellar clusters (Poveda et al. 1967; Leonard 1991; Bromley et al. 2009); ejection from star-forming dwarf galaxies, in particular it has been proposed that stars can be ejected from the Large Magellanic Cloud (LMC) with extremely large velocities (Boubert & Evans 2016); among others.

It is important to clarify that the different mechanisms eject stars with different velocities. While the Hills mechanism was initially proposed to explain stars with velocities exceeding 1000 km s^{-1} , the different interactions and mechanisms proposed above can produce stars with velocities as “low” as $\sim 400 \text{ km s}^{-1}$. Though the term HVS has initially been used to refer to unbound stars accelerated by Hills mechanism, it was also used to describe unbound stars and even stars with extreme velocities ($\sim 300 - 600 \text{ km s}^{-1}$) that are still bound to the Galactic Potential (Hattori et al. 2018b). In this paper we will use the term HVSs to describe extreme-velocity stars, but not necessarily unbound, nor stars that directly interacted with the central Sagittarius A* via the Hills mechanism.

From an observational perspective, only about 20 stars with extreme velocities were found prior to 2018 (Hattori et al. 2018b; Brown 2015). At that point, most of the HVSs were young, massive stars, such as B-type main sequence stars (e.g., Brown 2015, and references therein). These stars are believed to have been recently ejected from the Galactic Center, stellar disk, or star-forming dwarf satellites.

Opportunities to discover and characterize HVSs have considerably increased since the initial discoveries, especially owing to the Gaia data releases. For example, Shen et al. (2018) reported the discovery of three white dwarfs with velocities exceeding 1000 km s^{-1} , or the discovery of S5-HVS 1, an unbound A type star located at 9 kpc from the Sun travelling at a staggering 1700 km s^{-1} (Koposov et al. 2020; Irrgang et al. 2021). Bromley et al. (2018), Marchetti et al. (2018b,a), Boubert et al. (2018), and Hattori et al. (2018a) have all searched for

HVSs candidates, with a focus on late-type stars, and found over 30 stars.

The discovery of fast-moving late-type stars provides a powerful tool to study both the origin of HVSs and the mechanism that ejects stars to high velocities. While a chemical analysis of massive, young, A, O, and B-type stars is limited due to the high temperatures in the stellar photospheres, the analysis of late-type stars chemistry is far less complicated. The first work to study the chemistry of late-type HVSs was Hawkins & Wyse (2018). They did a comprehensive study of four extreme-velocity stars and found that all of them have chemical patterns consistent with Milky Way stars, and are part of the halo velocity distribution tail.

In this paper we continue the effort of carrying out a comprehensive spectroscopic analysis of HVSs. We observed 15 HVs candidates, updated their total velocities using Gaia EDR3 parallax and proper motions, and radial velocities from our high-resolution spectra, and performed a comprehensive chemical analysis of the targets. The paper is divided as follows: In Section 2 we outline our sample selection and observation, in Section 3 we describe how we estimated stellar parameters and orbits. We describe the chemical patterns of the stars in Section 4, discuss our results in Section 5 and provide our final remarks in Section 6.

2. SAMPLE SELECTION AND OBSERVATIONS

We analyzed a total of 15 stars. Our sample was selected from extreme-velocity stars from Hattori et al. (2018a) and Herzog-Arbeitman et al. (2018) (Gaia DR1 data). We selected stars that had quoted total velocities $\gtrsim 300 \text{ km s}^{-1}$, without previous spectroscopic analysis. A lack of a former spectroscopic analysis also mean their radial velocity estimates could be improved upon. We selected the targets, from the two studies above, based on their magnitudes (prioritizing brighter stars) and observability at the time of our observing runs. We also observed the well-known rapid neutron-capture process (r-process) enhanced star HE 1523–0901, which is also an extreme-velocity star. The extreme r-process enhancement of this star raises the interesting question of either or not other extreme-velocity stars are also r-process enhanced (Section 4.4).

We observed the targets with two instruments: the Magellan Inamori Kyocera Echelle (MIKE) spectrograph on the Magellan Clay Telescope at Las Campanas Observatory (Bernstein et al. 2003; Shectman & Johns 2003) and the ARC echelle spectrograph (ARCES) on the 3.5m Apache Point Observatory telescope. For MIKE observations we used either the $0''.35$ slit, the $0''.5$ slit or the $0''.7$ slit with standard blue and red grat-

ing azimuths, yielding spectra between 335 nm and 950 nm with resolving power varying from $R \approx 83,000$ to $R \approx 40,000$ in the blue arm and from $R \approx 65,000$ to $R \approx 31,000$ in the red arm. We collected all calibration data (e.g., bias, quartz & “milky” flat field, and ThAr lamp frames) in the afternoon before each night of observations. We reduced the raw spectra and calibration frames using the `CarPy`¹ software package (Kelson et al. 2000; Kelson 2003; Kelson et al. 2014). On ARCES, we used the standard 1′′6 slit yielding effective spectra with continuous coverage between 390 nm and 900 nm with resolving power of $R \approx 31,000$. All calibration data were collected prior to the science observations. We reduced ARCES data using the CERES pipeline (Brahm et al. 2017). We present a log of these observations in Table 1. We used `iSpec`² (Blanco-Cuaresma et al. 2014; Blanco-Cuaresma 2019) to calculate radial velocities and barycentric corrections and to normalize the spectra. Our estimated radial velocities are compatible with Gaia DR2 radial velocities, therefore we did not identify any signs of variability based on our data plus Gaia DR2.

3. ATMOSPHERIC PARAMETERS

The stellar parameters were obtained using the same method described in Reggiani et al. (2020, 2021) and Reggiani et al. (2022), a hybrid isochrone/spectroscopy approach. Isochrones are especially useful for effective temperature T_{eff} inferences in this case, as high-quality multiwavelength photometry is available for all stars. Similarly, the known distances, from Bailer-Jones et al. (2021) using Gaia EDR3 parallaxes (with uncertainties ≤ 0.05 mas), make the calculation of surface gravity $\log g$ via isochrones straightforward. We estimate the stellar microturbulent velocity using the empirical relation from Kirby et al. (2009).

To measure the stellar metallicity we use atomic data for Fe I and Fe II atomic absorption lines from Ji et al. (2020) and Reggiani & Meléndez (2018). The atomic and molecular data for the selected lines are from the `linemake` code³ (Sneden et al. 2009, 2016; Placco et al. 2021), maintained by Vinicius Placco and Ian Roederer. We first measure the equivalent widths of Fe I and Fe II atomic absorption lines by fitting Gaussian profiles with the `splot` task in IRAF to our continuum-normalized spectra. Whenever necessary, we use the `deblend` task

to disentangle absorption lines from adjacent spectral features. We report our input atomic data, measured equivalent widths, and line-abundances in Table 2.

We use 1D plane-parallel α -enhanced ATLAS9 model atmospheres (Castelli & Kurucz 2004), the 2019 version of the MOOG radiative transfer code (Sneden 1973), and the `q2 MOOG wrapper`⁴ (Ramírez et al. 2014) to derive stellar metallicities.

We use the `isochrones` package⁵ (Morton 2015) in an iterative process to self-consistently infer atmospheric and fundamental stellar parameters for each star using as input:

1. Gaia DR2 G magnitudes (Gaia Collaboration et al. 2016, 2018; Evans et al. 2018);
2. Distance prior from Bailer-Jones et al. (2021) and Gaia EDR3 parallaxes (Gaia Collaboration et al. 2016, 2020; Lindgren et al. 2020);
3. u , v , g , r , i , and z magnitudes and associated uncertainties from Data Release (DR) 2 of the SkyMapper Southern Sky Survey (Wolf et al. 2018) when available;
4. J , H , and K_s magnitudes and associated uncertainties from the 2MASS PSC (Skrutskie et al. 2006);
5. $W1$, and $W2$ magnitudes and associated uncertainties from the Wide-field Infrared Survey Explorer (WISE) AllWISE Source Catalog (Wright et al. 2010; Mainzer et al. 2011);
6. A_V extinction from the Bayestar2019 3D extinction maps (Green et al. 2019);

We use `isochrones` to fit the MESA Isochrones and Stellar Tracks (MIST; Dotter 2016; Choi et al. 2016; Paxton et al. 2011, 2013, 2015) library to these data using `MultiNest`⁶ (Feroz & Hobson 2008; Feroz et al. 2009, 2019) through `PyMultiNest` (Buchner et al. 2014). We restricted the MIST library based on the photometric distances from Bailer-Jones et al. (2021), and extinction A_V in the range $0 \leq A_V$ (mag) ≤ 0.3 , based on the A_V values and errors proposed by the 3D extinction maps of Green et al. (2019).

We first use `isochrones` to find self-consistent and physically motivated effective temperature and surface gravity results. Using the inferred $\log g$ we estimate the

¹ <http://code.obs.carnegiescience.edu/mike>

² <https://www.blancocuaresma.com/s/iSpec>

³ <https://github.com/vmplacco/linemake>

⁴ <https://github.com/astroChasqui/q2>

⁵ <https://github.com/timothydmorton/isochrones>

⁶ <https://ccpforge.cse.rl.ac.uk/gf/project/multinest/>

Table 1. Log of Observations

Source ID	R.A.	Decl.	UT Date	Start	Slit	Exposure	S/N	S/N	Instrument
EDR3	(h:m:s)	(d:m:s)			Width	Time (s)	4500 Å	6500 Å	
2853089398265954432	00 00 21.88	+25 19 21.81	2018 Oct 26	6:00:13	1.6	870	35	55	ARCES
330414789019026944	01 56 52.65	+36 39 57.89	2018 Oct 28	5:48:53	1.6	1200	78	123	ARCES
2260163008363761664	18 07 53.09	+70 12 47.92	2018 Oct 28	2:05:55	1.6	1300	66	104	ARCES
2233912206910720000	19 57 21.65	+55 30 23.00	2018 Oct 28	2:36:30	1.6	4110	41	65	ARCES
1765600930139450752	21 49 48.66	+10 48 43.08	2018 Oct 26	5:26:18	1.6	1350	35	55	ARCES
3252546886080448384	04 09 02.19	-02 12 27.07	2018 Nov 16	3:53:10	0.5	1000	86	118	MIKE
5212110596595560192	06 16 51.67	-78 26 20.78	2018 Nov 16	8:30:20	0.5	300	56	115	MIKE
5212817273334550016	07 08 47.74	-76 13 10.16	2018 Nov 16	8:36:53	0.5	400	63	126	MIKE
3599974177996428032	11 44 40.87	-04 09 51.27	2018 Jan 25	7:28:56	0.7	600	110	198	MIKE
6317828550897175936	15 26 01.07	-09 11 38.88	2017 Aug 25	1:42:34	0.7	600	91	210	MIKE
6479574961975897856	21 05 58.65	-49 19 33.51	2017 Aug 17	4:12:25	0.35	3030	296	342	MIKE
6558932694746826240	21 55 50.81	-51 05 37.21	2017 Aug 17	2:49:14	0.7	600	104	178	MIKE
2629296824480015744	22 23 19.86	-02 31 10.61	2018 Nov 16	1:12:31	0.5	450	76	122	MIKE
6505889848642319872	22 47 40.24	-55 37 31.43	2018 Nov 16	1:22:18	0.5	300	85	145	MIKE
6556192329517108352	23 08 00.95	-33 38 06.94	2017 Aug 17	3:01:00	0.7	600	97	180	MIKE

microturbulent velocity ξ using the empirical relation from Kirby et al. (2009). We impose the T_{eff} , $\log g$, and ξ inferred in this way to derive $[\text{Fe}/\text{H}]$. The metallicities are inferred exclusively from Fe II lines, as they are less affected by non-LTE effects. Though at times there are non negligible differences between Fe I and Fe II inferred abundances we adopt the $[\text{Fe II}/\text{H}]$ ratios as our model metallicity. We then execute another **isochrones** calculation, this time using this updated set of atmospheric stellar parameters in the likelihood. We iterate this process until the metallicities inferred from both the **isochrones** analysis and the equivalent widths analysis are consistent (i.e., the isochrone metallicity is the same as the spectroscopic within the uncertainties found by the isochrone analysis, which is typically on the order of 0.1 dex). The adopted stellar parameters are presented in Table 3.

We derive the uncertainties in our adopted $[\text{Fe}/\text{H}]$ and ξ values due to the uncertainties in our adopted T_{eff} and $\log g$ values using a Monte Carlo simulation. We randomly sample 200 self-consistent pairs of T_{eff} and $\log g$ from our **isochrones** posteriors and calculate the values of $[\text{Fe}/\text{H}]$ and ξ . We save the result of each iteration and find that the contributions of T_{eff} and $\log g$ uncertainties to our final $[\text{Fe}/\text{H}]$ and ξ uncertainties are not relevant.

The random uncertainties derived via isochrones are under the unlikely assumption that the MIST isochrone grid perfectly reproduces all stellar properties. There are almost certainly larger systematic uncertainties that

we have not investigated. To account for them we adopted the conservative photospheric stellar parameters uncertainties of $\Delta T_{\text{eff}} = 100$ K and $\Delta \log g = 0.15$ for the isochrone-based parameters. As a change of 0.15 dex in surface gravity only changes our estimated microturbulences by 0.03 km s^{-1} , we conservatively adopted an uncertainty of $\Delta \xi = 0.1 \text{ km s}^{-1}$. The reported metallicity uncertainties were derived by adding in quadrature the uncertainties from our line-by-line abundance dispersions and the T_{eff} , $\log g$, and ξ adopted uncertainties. We report our derived stellar parameters, along with the stellar photometric and astrometric data, in Table 3.

One of our targeted stars, identified here as Gaia EDR3 6317828550897175936, is the well-known r-process enhanced metal-poor star HE 1523-0901 (Frebel et al. 2007). We use this star to roughly quantify the systematics generated by our methodology. Based on our isochrone analysis combined with the Fe II lines, we derived the following stellar parameters for HE 1523-0901: $T_{\text{eff}} = 4742 \pm 100$ K, $\log g = 1.29 \pm 0.15$, $[\text{Fe}/\text{H}] = -2.65 \pm 0.22$, and $\xi = 1.83 \pm 0.10 \text{ km s}^{-1}$.

Frebel et al. (2007) derived $T_{\text{eff}} = 4630 \pm 40$ K, $\log g = 1.0 \pm 0.3$, $[\text{Fe}/\text{H}] = -2.95 \pm 0.20$, and $\xi = 2.63 \pm 0.3 \text{ km s}^{-1}$. Their effective temperature was derived applying the Alonso et al. (1999) calibration from BVRI photometry. Surface gravity, metallicity, and microturbulent velocity were derived via the classic spectroscopic method. Despite the differences in our analysis meth-

ods the derived stellar parameters are fully compatible within the proposed analyzes uncertainties.

A more recent analysis of this star was performed by Casey et al. (2017) using a data-driven analysis of RAVE (Kunder et al. 2017) data using *The Cannon* (Ness et al. 2015, 2016) pipeline. They reported $T_{\text{eff}} = 4789 \pm 108$ K, $\log g = 1.54 \pm 0.23$, and $[\text{Fe}/\text{H}] = -2.56 \pm 0.09$. These recent results are very similar to our derived photospheric parameters. Our method to determine the stellar parameters are in agreement with the most recent data-driven methods.

Finally we compare our results for this star to Sakari et al. (2018), who derived $T_{\text{eff}} = 4530$ K, $\log g = 0.8$, $[\text{Fe}/\text{H}] = -2.72$, and $\xi = 2.26$ km s⁻¹. Their stellar parameters were estimated using a differential spectroscopic analysis, taking into account $\langle 3D \rangle$ non-LTE corrected iron abundances. In their paper Sakari et al. (2018) estimates uncertainties to be on the order of 20-200 K for effective temperature, 0.05-0.3 dex in surface gravity, and 0.10-0.35 in microturbulent velocity. Therefore their results are also compatible with our derived stellar parameters.

In summary, our method is compatible with a recent, well tested, data-driven method and also consistent with the more classical approach from Frebel et al. (2007). There is a larger difference between our work and that of Sakari et al. (2018) but it can be accounted by the uncertainties. All four studies briefly discussed here were performed with fundamentally different techniques but they obtain similar results within their uncertainties. We can conclude that our methodology can be directly compared with the above-mentioned results and that our adopted uncertainties are reasonable.

3.1. Stellar Orbits

We calculated the Galactic orbits of our sample stars using `galpy`⁷. `Galpy` uses a left-handed coordinate system, with the Sun at positive X and positive L_Z indicates a prograde orbit. We sampled 1,000 Monte Carlo realizations from the Gaia EDR3 astrometric solutions for each star using the distance posterior that results from our isochrone analysis while taking full account of the covariances between position, parallax, and proper motion. We used the radial velocities derived from our spectra and assumed no covariance between our measured radial velocity and the Gaia EDR3 astrometric solution. We used each Monte Carlo realization as an initial condition for an orbit and integrated it forward 10 Gyr in a Milky Way-like potential. We adopted the

`MWPotential2014` described by Bovy (2015). In that model, the bulge is parameterized as a power-law density profile that is exponentially cut-off at 1.9 kpc with a power-law exponent of -1.8 . The disk is represented by a Miyamoto–Nagai potential with a radial scale length of 3 kpc and a vertical scale height of 280 pc (Miyamoto & Nagai 1975). The halo is modeled as a Navarro–Frenk–White halo with a scale length of 16 kpc (Navarro et al. 1996). We set the solar distance to the Galactic center to $R_0 = 8.122$ kpc, the circular velocity at the Sun to $V_0 = 238$ km s⁻¹, the height of the Sun above the plane to $z_0 = 25$ pc, and the solar motion with the respect to the local standard of rest to $(U_\odot, V_\odot, W_\odot) = (10.0, 11.0, 7.0)$ km s⁻¹ (Jurić et al. 2008; Bland-Hawthorn & Gerhard 2016; Gravity Collaboration et al. 2018). We report the resulting orbital parameters (radial velocities, total galactic velocities v , pericenter R_{peri} , apocenter R_{apo} , eccentricity e , maximum distance from the galactic plane Z_{max} , total orbital energy E_{tot} , and angular momentum L_Z) in Table 3.

4. CHEMICAL ABUNDANCES

We measured the equivalent widths of atomic absorption lines for Na I, Mg I, Al I, Si I, K I, Ca I, Sc II, Ti I, Ti II, Cr I, Cr II, Mn I, Fe I, Fe II, Co I, Cu I, Ni I, Zn I, Sr I, Sr II, Y II, Ba II, and La II, in our continuum-normalized spectra by fitting Gaussian profiles with the `splot` task in `IRAF`. We used the `deblend` task to disentangle absorption lines from adjacent spectral features whenever necessary. We employed the 1D plane-parallel α -enhanced ATLAS9 model atmospheres and the 2019 version of `MOOG` to calculate abundances for each equivalent width. We report our input atomic data from Ji et al. (2020) and Reggiani & Meléndez (2018). The atomic and molecular data are from the `linemake` code (Snedden et al. 2009, 2016; Placco et al. 2021). We measured equivalent widths, and individual inferred abundances in Table 2. We measured Eu abundances from Eu II lines through spectrum synthesis, from up to five lines: 4129, 4205, 4435, 4522, and 6645 Å. We present our adopted mean chemical abundances, and associated errors, in Table 4. The $\sigma_{[\text{X}/\text{Fe}]}$ are a measure of the line dispersion divided by the number of lines, added in quadrature to the uncertainties due to the adopted stellar parameters uncertainties ($\Delta T_{\text{eff}} = 100$ K, $\Delta \log g = 0.15$ cm.s⁻², and $\xi = 0.1$ km s⁻¹). We show our abundances, with data from additional bibliographical sources in Figures 1 to 4. In Figures 1 through 4 we use the more commonly employed mean value of all Fe I and Fe II lines to estimate the $[\text{X}/\text{Fe}]$ ratios and for the $[\text{Fe}/\text{H}]$ ratio. Though it differs from our model

⁷ <https://github.com/jobovy/galpy>

metallicities, these $[\text{Fe}/\text{H}]$ ratios and $[\text{X}/\text{Fe}]$ ratios are directly comparable to the literature data.

To quantify possible systematics we compared our derived abundances for star HE 1523–0901 with those from Sakari et al. (2018). We chose Sakari et al. (2018) because neither Frebel et al. (2007) nor Casey et al. (2017) provided full sets of abundances for this star, and because Sakari et al. (2018) also calculated most abundances from equivalent widths and used the same radiative transfer code (MOOG).

We found a mean absolute abundance difference of $\Delta[\text{X}/\text{Fe}] = -0.14$ dex. This value is well within the errors of the analyzes. HE 1523–0901 is known to be highly r-process enhanced, and our inferred neutron-capture process elemental abundances are, as expected, enhanced. There is a difference when we compare our results to those inferred by Sakari et al. (2018): $\Delta[\text{Y}/\text{Fe}] = -0.16$, $\Delta[\text{Ba}/\text{Fe}] = -0.3$, $\Delta[\text{Eu}/\text{Fe}] = 0.07$, and $\Delta[\text{La}/\text{Fe}] = -0.24$. These differences are mostly due to the fact that our mean metallicity (derived from Fe I and Fe II lines) is higher than adopted in their work. Instead, if our Fe II $[\text{Fe II}/\text{H}]$ is used to estimate $[\text{X}/\text{Fe}]$ the differences are considerably reduced: $\Delta[\text{Y}/\text{Fe}] = 0.04$, $\Delta[\text{Ba}/\text{Fe}] = 0.1$, $\Delta[\text{Eu}/\text{Fe}] = -0.01$, and $\Delta[\text{La}/\text{Fe}] = 0.04$.

Although there are non-negligible differences in a few elements, they are on the order of the inferred uncertainties, as evidenced by our mean abundance difference (from Sakari et al. 2018). We conclude that any systematics in our analysis are lower than about ~ 0.2 dex and are accounted for in our uncertainties.

4.1. α -Elements

In Figure 1 we show the chemical abundances of the α -elements (Mg, Si, Ca, and Ti - elements synthesized through α reaction, and Ti, which is not formed through the same nucleosynthetic channel but is often considered to be an α -element due to its chemical abundances similarities). These elements indicative of how fast chemical evolution took place in any given environment. This can be done via the “knee”, an inflection in $[\alpha/\text{Fe}]$ indicating “when” iron production start to be dominated by type Ia supernovae instead of type II supernovae. The position of the knee ultimately depends on the complex details of the star formation history in a given environment, but as a general rule it can be associated with the mass of the host galaxy (e.g., Tinsley 1979; Matteucci & Brocato 1990; Suda et al. 2017).

In the Milky Way the position of the “knee” is at $[\text{Fe}/\text{H}] \sim -1.0$ and the evolution of the $[\alpha/\text{Fe}]$ abundances is well understood. Below the position of the knee there is an abundance plateau in the α -abundances

that spans all the metallicity range of our study. The abundance plateau, for metallicities lower than $[\text{Fe}/\text{H}] \leq -1.0$, is observed to be at ~ 0.3 dex for $[\text{Mg}/\text{Fe}]$, $[\text{Si}/\text{Fe}]$, and $[\text{Ca}/\text{Fe}]$. However, models diverge from the observations and predict a plateau at $[\text{Mg}/\text{Fe}] \sim 0.45$ dex, $[\text{Si}/\text{Fe}] \sim 0.5$ dex, and $[\text{Ca}/\text{Fe}] \sim 0.3$ dex (e.g. Tinsley 1979; Matteucci & Brocato 1990; Reggiani et al. 2017; Hayes et al. 2018; Amarsi et al. 2020; Kobayashi et al. 2020a, to cite a few).

The HVSs analyzed by Hawkins & Wyse (2018) all had Galactic chemistry. Their α -abundances were typical high- α halo stars, with metallicities between $-2 \leq [\text{Fe}/\text{H}] \leq -1$. In Figure 1 we show our α -abundance ratios, along with different bibliographic samples of the Milky Way halo (Cayrel et al. 2004; Nissen & Schuster 2010; Reggiani et al. 2017), Milky Way thick disk (Nissen & Schuster 2010), Milky Way bulge (Bensby et al. 2010), and the dwarf galaxies Carina (Shetrone et al. 2003), Sculptor (Shetrone et al. 2003; Geisler et al. 2005), Sagittarius (Monaco et al. 2005), and Fornax (Letarte et al. 2010).

At metallicities higher than $[\text{Fe}/\text{H}] \gtrsim -1.5$, our mean abundances are $[\text{Mg}/\text{Fe}] = 0.1$ dex, $[\text{Ca}/\text{Fe}] = 0.2$ dex, $[\text{Si}/\text{Fe}] = 0.3$ dex, and $[\text{Ti}/\text{Fe}] = 0.2$ dex. Apart from silicon abundances, for which non-LTE effects can be important at the measured lines, all our α -elements have abundances consistently lower than the observed Milky Way plateau, and considerably lower than the chemical evolution models predict (Kobayashi et al. 2020a). These abundances are consistent with abundances of stars formed after the knee, which is expected to be at lower metallicities for lower-mass galaxies (Suda et al. 2017). In Figure 1 we can also visibly infer that the α -abundances for these 5 stars are on top of either the dwarf galaxies abundances or the Nissen & Schuster (2010) low- α sequence, which are also interpreted as accreted stars. This is particularly true for the two highest metallicity stars. The other three stars have somewhat higher calcium abundances, but as can be seen in Figure 1 the calcium dispersion is not as high and the low- and high- α sequences from Nissen & Schuster (2010) are not as distinguishable as they are in the magnesium ratios. Therefore, their α -abundance ratios are more consistent with those found in dwarf galaxies.

At metallicities lower than $[\text{Fe}/\text{H}] \lesssim -1.5$ our mean abundances are different: $[\text{Mg}/\text{Fe}] = 0.2$ dex, $[\text{Si}/\text{Fe}] = 0.2$ dex, $[\text{Ca}/\text{Fe}] = 0.3$ dex, and $[\text{Ti}/\text{Fe}] = 0.2$ dex. Again, as silicon might be affected by non-LTE effects, our main indicators are the higher magnesium and calcium abundances, consistent with Milky Way studies. It is also important to point that the stars with the lowest α -abundances below $[\text{Fe}/\text{H}] \leq -1.5$ also have the largest

uncertainties. Although we have stars at this metallicity range that are compatible with the low- α sequence (Nissen & Schuster 2010) and can be accreted stars, the overall behavior at lower metallicities is more similar to Milky Way stars. It is also important to remark that the scatter at lower metallicities is higher (see the Cayrel et al. (2004) abundance spread compared to the Reggiani et al. (2017) and Nissen & Schuster (2010) spread at Figure 1, for example).

To summarize, our α -abundances indicate that the high metallicity end of our sample is likely composed of accreted stars, while the low-metallicity sample is more likely to be Milky Way in situ stars, apart from a couple of stars with higher uncertainties that could also be accreted stars. The chemical abundances of additional elements will provide further information regarding the stellar origin.

4.2. Light odd-Z

Figure 2 shows the abundances of the light odd-Z elements (Na, Al, K, and Sc).

While sodium and aluminum are mostly produced in core-collapse supernovae, their yields are dependent on metallicity and consequently their chemical evolution is not as easily interpreted as the chemical evolution of the α -elements. Both the exact nucleosynthetic origin and chemical evolution of scandium and potassium are likewise hard to identify and interpret (e.g., Clayton 2007; Zhao et al. 2016; Prantzos et al. 2018; Reggiani et al. 2019; Kobayashi et al. 2020a). We plot in the top panels of Figure 2 our measured [Na/Fe] and [Al/Fe], and [K/Fe] and [Sc/Fe] abundances as a function of [Fe/H] on the lower panels.

Sodium, aluminum and potassium abundance inferences can be strongly affected by departures from LTE, but scandium abundances from Sc II lines are not strongly affected (Zhao et al. 2016). We corrected sodium abundances using the Lind et al. (2011) grid through the INSPECT project⁸. The aluminum non-LTE abundance corrections are from Nordlander & Lind (2017). We obtained potassium abundance corrections via a linear interpolation of the Reggiani et al. (2019) grid of corrections for abundances inferred from the equivalent width of the K I line at 7698 Å.

As already found for the α -elements the abundance ratios of sodium, aluminum and potassium are lower for the higher metallicity stars. Particularly for sodium we can see that the abundance of our high metallicity stars are closer to the abundances in dSphs than the

abundances in the Milky Way. Scandium abundances are near [Sc/Fe] \sim 0.0 with a scatter, similar to the stars both in the Milky Way and dwarf galaxies.

4.3. Iron-peak elements

Iron-peak elements are mostly synthesized in type Ia supernovae explosions, and their abundance pattern typically follow that of iron. In Figure 3 we show our iron-peak [X/Fe] ratios (Cr, Mn, Ni, and Zn).

Chromium abundances were calculated both from Cr I and Cr II lines and both abundances are presented in Table 4. In Figure 3, we show the results for Cr I. The chromium abundances are scattered, but follow the same abundance path with increasing metallicity that is observed in other samples based on Cr I lines. At higher metallicities the stars also appear to have abundances that overlap with those observed in dwarf galaxies.

The other iron-peak elements diverge more from the Milky Way. At lower metallicities the inferred manganese abundances are compatible with the abundances of the Milky Way, but the abundances of the more metal-rich stars are lower than in the Milky Way. Other than our target stars, in Figure 3, there are few stars with very low manganese abundances, and all of them are from dwarf galaxies. The same happens for nickel and zinc. It is particularly interesting that we find low [Ni/Fe] ratios, because in Milky Way stars nickel abundances are [Ni/Fe] \sim 0.0 regardless of the stellar metallicity because its enrichment history is extremely well tied to that of iron. This is exemplified in Reggiani et al. (2017), who showed the extremely tight correlation of nickel abundances in the solar neighborhood. On the other hand there is considerable scatter in the nickel abundances of dwarf galaxies. This is tied to the different nucleosynthetic sources expected for the Milky Way and dwarf galaxies. While a large enrichment from sub-Chandrasekhar mass type Ia explosions (lower nickel production) is observed for dwarf galaxies, in the Milky Way the enrichment is dominated by Chandrasekhar-mass type Ia explosions (larger nickel production, e.g., Kobayashi et al. 2020b). Zinc in the Milky Way is also defined by an increase in the abundance ratio as metallicity decreases. This is associated with higher explosion energies of type II supernovae at earlier times (Kobayashi et al. 2020a). On the other hand, high explosion energies in dwarf galaxies, where the gravitational potential is shallow, might cause the gas to leave the galaxy and the observed abundances of the next generation of stars do not include this high zinc signature as it does in the Milky Way. Therefore, the abundance ratios of [Ni/Fe] and [Zn/Fe] are strong evidence of the extragalactic origin of these stars.

⁸ <http://inspect-stars.com/>

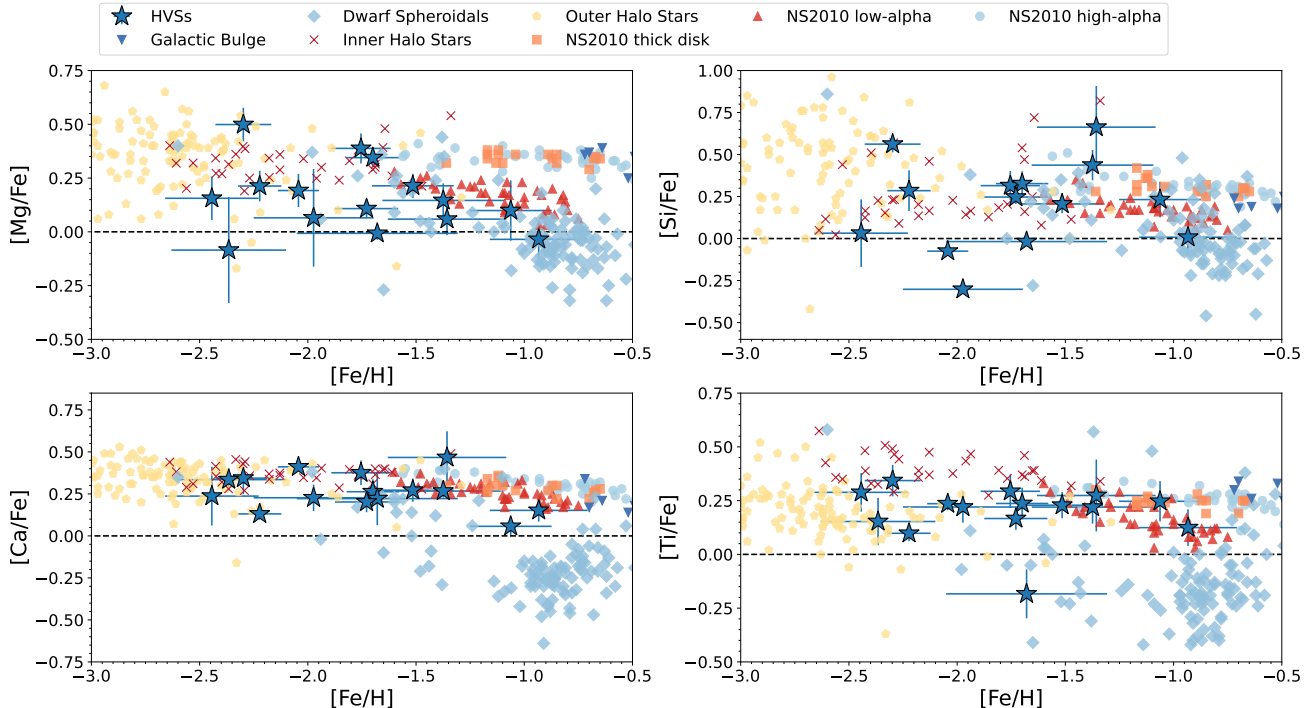


Figure 1. Abundances of the α -elements magnesium, silicon, and calcium, and titanium. We plot our HVs as dark-blue stars. We plot in yellow the abundances of Milky Way metal-poor stars from Cayrel et al. (2004) and Jacobson et al. (2015) outer halo stars; in red we show abundances of inner halo stars from Reggiani et al. (in prep), Reggiani et al. (2017) and Nissen & Schuster (2010); we display the Bensby et al. (2010) bulge stars in orange; in light-blue we include stars from the dwarf spheroidal galaxies Carina, Sculptur, Fornax, and Sagittarius from Shetrone et al. (2003), Geisler et al. (2005), Monaco et al. (2005), and Letarte et al. (2010).

4.4. Neutron capture elements

We also measured neutron-capture elements (Sr, Y, Ba, La, and Eu), and we show our abundances in Figure 4. We show the Sr II abundances because they are not strongly affected by non-LTE effects (Hansen et al. 2013). Yttrium abundances were estimated using hyperfine structure data from the Kurucz⁹ linelists. Barium abundances were calculated using the isotopic splitting from McWilliam (1998) and Klose et al. (2002). Europium abundances were estimated using spectral synthesis from up to 5 lines (4129, 4205, 4435, 4522 and 6645 Å).

Contrary to what we saw so far for the α , light-odd, and iron-peak elements, the abundances of the neutron-capture elements Y and Ba are supersolar for the high metallicity stars in our sample. This is compatible with the observed patterns of extragalactic environments, but not with extreme r-process enhancement found, for example, in the ultra-faint dwarf galaxy Reticulum II Ji et al. (2016). The europium in our sample is not highly enhanced. The r-process distribution of our sample is

similar to the Milky Way r-process abundance distribution, with the exception of HE 1523–0901 which was already known to have $[\text{Eu}/\text{Fe}] > 1.7$ dex. Again, it indicates our stars are not from an extreme environment such as Reticulum II.

5. DISCUSSION

5.1. Stellar Origin

We observed 15 extreme-velocity stars with either MIKE/Magellan or ARCES at the 3.5m Apache Point observatory. The chemical abundances ($[\alpha]$, iron-peak, and neutron-capture/Fe) ratios) of our sample of extreme-velocity stars indicate that at least 50% of our sample are of extragalactic origin (these stars are identified by a *c* at the External ID field of Table 3).

The stars that do have more similarities with Milky Way chemical abundances are at the low metallicity end of our sample. In particular the three most metal-poor stars we analyzed have chemical abundances more consistent with Milky Way halo stars, (high- α and slow neutron-capture scattered around ~ 0.0). Their light odd-Z abundances, and in particular the iron-peak $[\text{Mn}/\text{Fe}]$ and $[\text{Ni}/\text{Fe}]$ abundances are Milky Way-like. There are stars at the low-metallicity end that have

⁹ <http://kurucz.harvard.edu/linelists.html>

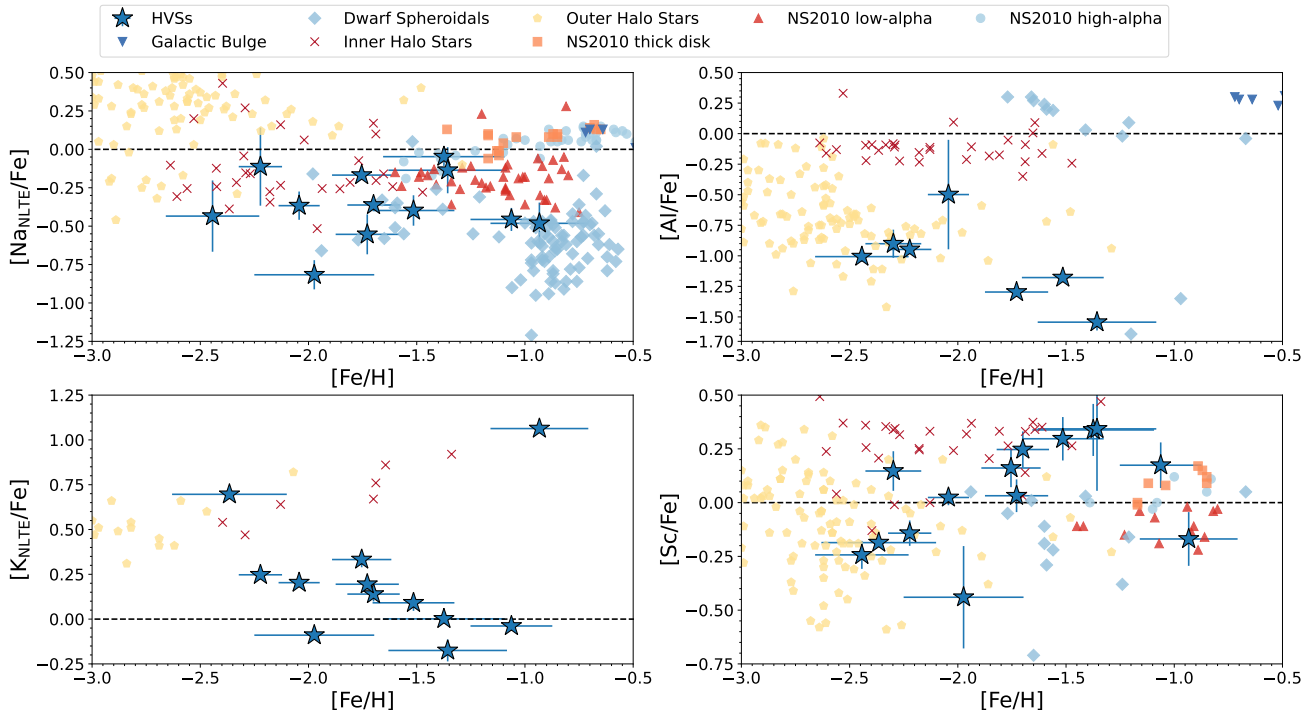


Figure 2. Abundances of the light odd-Z elements sodium, aluminum, potassium and scandium. We plot our HVSSs as dark-blue stars. We plot in yellow the abundances of Milky Way metal-poor stars from Cayrel et al. (2004) and Jacobson et al. (2015) outer halo stars; in red we show abundances of inner halo stars from Reggiani et al. (in prep), Reggiani et al. (2017), Nissen & Schuster (2010), and ?; we display the Bensby et al. (2010) bulge stars in orange; in light-blue we include stars from the dwarf spheroidal galaxies Carina, Sculptur, Fornax, and Sagittarius from Shetrone et al. (2003), Geisler et al. (2005), Monaco et al. (2005), and Letarte et al. (2010).

low $[\text{Ni}/\text{Fe}]$ abundances but Milky Way-like abundances of other species, and the nickel abundance alone is not enough evidence of an extragalactic origin. As was concluded by Hawkins & Wyse (2018) for their sample, these stars are also consistent with the tail of the velocity distribution of the Milky Way.

The chemical abundances of the high metallicity end of the sample ($[\text{Fe}/\text{H}] \gtrsim -1.5$) resemble the chemical patterns of stars formed in other galaxies, in particular the low $[\alpha/\text{Fe}]$ ratios, and high $[\text{s-process}/\text{Fe}]$ ratios. The knee of the Milky Way, the position in $[\text{Fe}/\text{H}]$ space where there is an inflection in $[\alpha/\text{Fe}]$ towards $[\alpha/\text{Fe}] \leq 0.0$, is known to be at $[\text{Fe}/\text{H}] = -1.0$ (e.g., Matteucci & Brocato 1990; Suda et al. 2017). Therefore, stars with near-solar or sub-solar α abundances below or close to that $[\text{Fe}/\text{H}] = -1.0$ are likely to have formed in another galaxy.

These conclusions can be made exclusively based on the α -elements because their abundances in our targets stars are extremely informative. Nevertheless, the abundances of Na, Al, Mn, Ni, Zn, Y, and Ba in our higher metallicity stars also show signatures that diverge from the behavior found in Milky Way stars.

In particular, their $[\text{Mn}/\text{Fe}]$, $[\text{Ni}/\text{Fe}]$, and $[\text{Zn}/\text{Fe}]$ are very diagnostic. Both de los Reyes et al. (2020) and Sanders et al. (2021) analyzed extragalactic stars and studied the enrichment of iron-peak elements via sub-Chandrasekhar Type Ia supernovae. While de los Reyes et al. (2020) used medium resolution spectra to study stars in dwarf galaxies, Sanders et al. (2021) used high-resolution results from the literature and APOGEE to study the chemical history of the Gaia-Enceladus-Sausage. Both studies concluded that the dominant mechanism of iron-peak enrichment in dwarf galaxies is the sub-Chandrasekhar type Ia supernova. Sanders et al. (2021) also looked at $[\text{Ni}/\text{Fe}]$ and $[\text{Zn}/\text{Fe}]$ and found both are sub-solar and indicative of substantive sub-Chandrasekhar mass enrichment. We see in our stars the same qualitative behavior, meaning sub-solar abundances of these three key elements. However, our abundances, manganese in particular, are lower than those reported by the studies above and our sample is not monotonically selected to have been formed in the same dwarf galaxy/Galactic structure. Therefore it is difficult to make further conclusions regarding their type Ia supernova enrichment history. We can say though that near-Chandrasekhar or Chandrasekhar

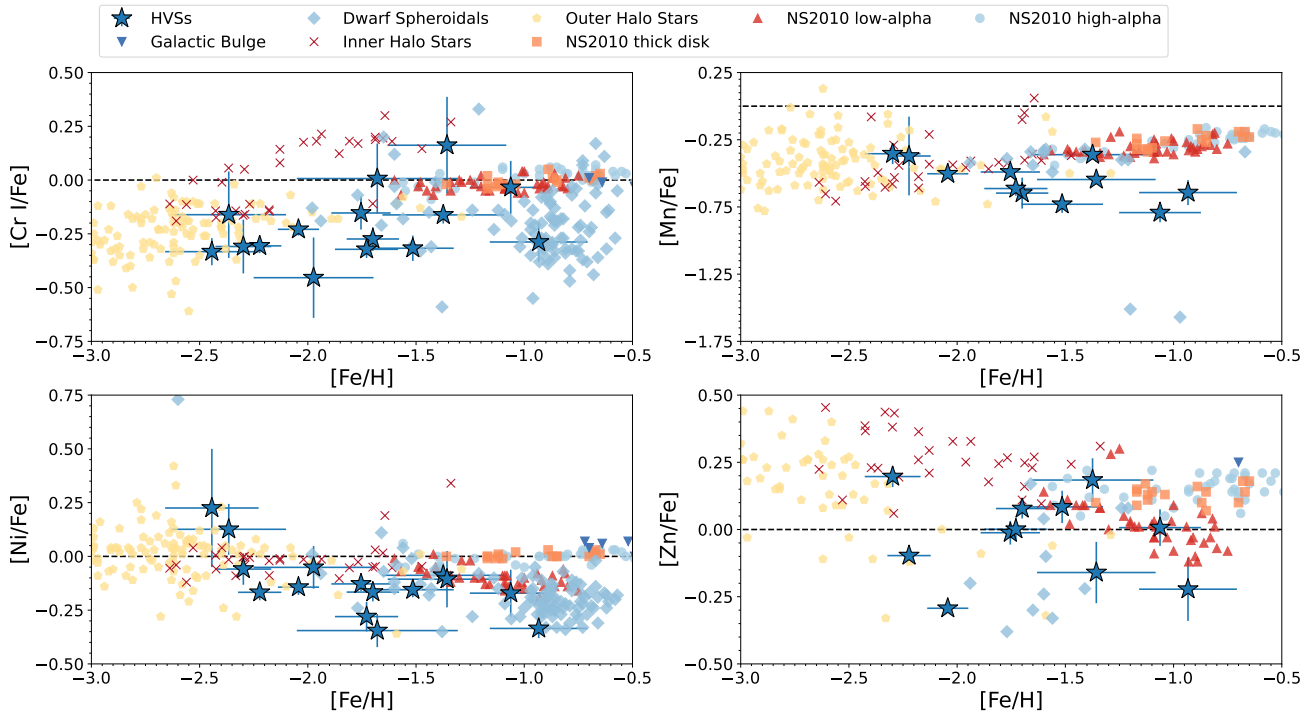


Figure 3. Abundances of the iron-peak elements chromium, manganese, nickel, and zinc. We plot our HVs as dark-blue stars. We plot in yellow the abundances of Milky Way metal-poor stars from Cayrel et al. (2004) and Jacobson et al. (2015) outer halo stars; in red we show abundances of inner halo stars from Reggiani et al. (in prep), Reggiani et al. (2017) and Nissen & Schuster (2010); we display the Bensby et al. (2010) bulge stars in orange; in light-blue we include stars from the dwarf spheroidal galaxies Carina, Sculptur, Fornax, and Sagittarius from Shetrone et al. (2003), Geisler et al. (2005), Monaco et al. (2005), and Letarte et al. (2010).

mass thermonuclear explosions would yield larger manganese, nickel, and zinc abundances (see, e.g., Reggiani et al. 2020), and we are therefore seeing contributions from sub-Chandrasekhar mass type Ia supernovae.

Further evidence of extragalactic origin for our HVs sample come from their kinematics. We used the kinematic and astrometric data (Gaia EDR3 parallaxes and proper motions), distances estimated from our isochrones posteriors (compatible with the Bailer-Jones et al. (2021) prior-informed distances) and radial velocities from our spectra to calculate their orbital parameters and substructure membership probabilities. In Figure 5 we show their total energy as a function of angular momentum. We also show in that figure the Galactic substructures as identified in Naidu et al. (2020). All our targets have quite different kinematic properties from the known substructures and the estimated membership probabilities are likely unreliable.

This is not unexpected as they were selected to have higher velocities and therefore higher energies. It is surprising, though, to see at least two separate clusters of stars in the angular momentum plane. Assuming these stars did not originate in the Milky Way we can assume that the stars clustered around $L_z < 0.55 \times 10^3$ kpc km

s^{-1} were accreted to the galaxy during a radial accretion event. The clustering at higher L_z is more difficult to explain. This could hint to a previously unidentified substructure, a hypothesis that would be compatible with our chemical results, but we do not have enough data (stars) to conclude it, and our data is biased because we only targeted high velocity stars. We also do not see any sign of one clear substructure in our velocities distribution. We see stars that are both rotation in the same direction and in the opposite direction as the galactic rotation. This is not unexpected and can be attributed to the selection of our targets. We just selected for total velocity, and did not search for substructures in the data.

Additionally we show in Figure 6 the maximum distance from the Galactic plane as a function of eccentricity for the stars in our sample. We compare our results to those of Necib et al. (2020), which include Galactic Halo stars, Enceladus Stars and stars from the Nyx stream. We can see that a few stars from our sample clearly deviate from our comparison data. The high eccentricities, along with the large total distances from the Galactic plane are yet another evidence of accretion. While a few stars are compatible with the halo sample,

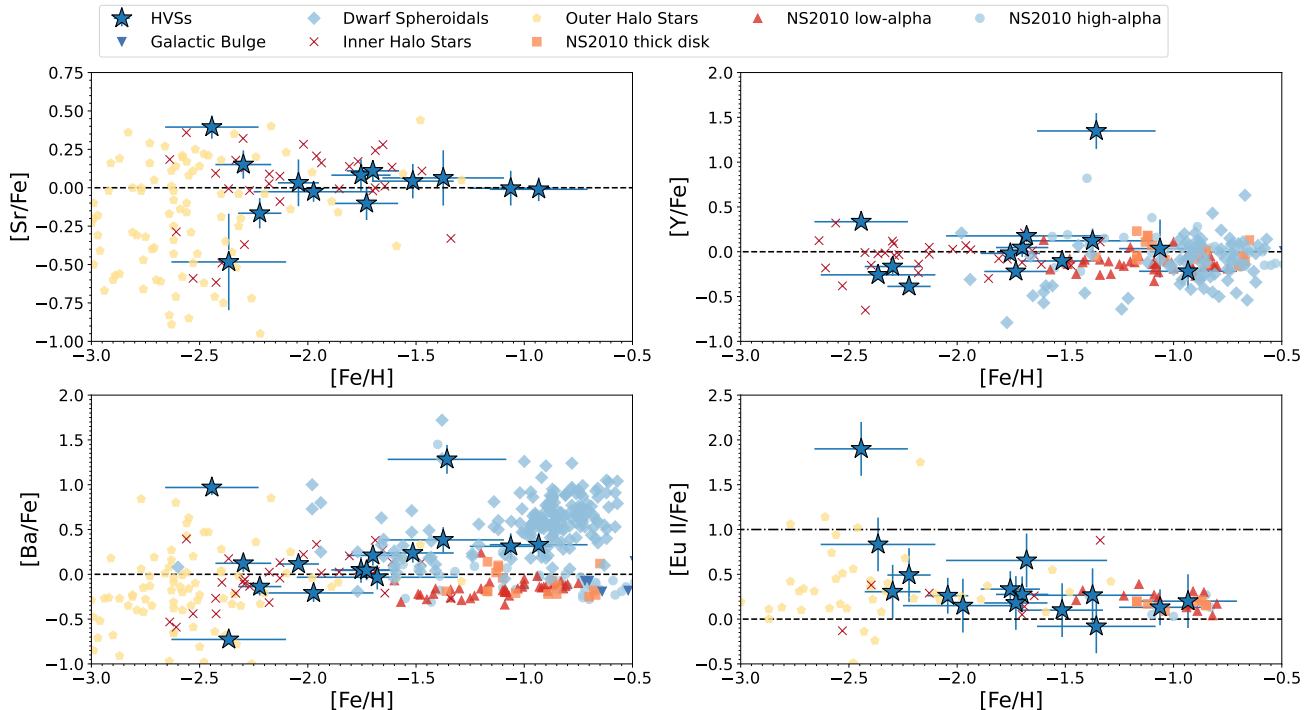


Figure 4. Abundances of the neutron capture elements strontium, yttrium, and barium. We plot our HVSSs as dark-blue stars. We plot in yellow the abundances of Milky Way metal-poor stars from Cayrel et al. (2004) and Jacobson et al. (2015) outer halo stars; in red we show abundances of inner halo stars from Reggiani et al. (in prep), Reggiani et al. (2017) and Nissen & Schuster (2010); we display the Bensby et al. (2010) bulge stars in orange; in light-blue we include stars from the dwarf spheroidal galaxies Carina, Sculptur, Fornax, and Sagittarius from Shetrone et al. (2003), Geisler et al. (2005), Monaco et al. (2005), and Letarte et al. (2010).

in particular those with smaller eccentricities, most stars in our sample could have been accreted (like Enceladus stars). There is a caveat that the eccentricities and large distances from the Galactic plane could have originated if a star is “kicked” through some mechanism, being accelerated by, for example, a supernova explosion. This is yet another evidence pointing these stars are likely accreted stars.

We also remark that our calculations did not include the Magellanic Clouds potential and we are unable to infer a probability of one of the stars having originated from the Large Magellanic Cloud (LMC). According to Evans et al. (2021) the LMC can be an important source of hypervelocity stars, particularly for “lower” velocity stars, and could contribute more than the Galactic center to the number of observed HVSSs, but so far only one HVS star has been confirmed to have originated in the LMC (Erkal et al. 2019). Evans et al. (2021) also points that the high-velocity tail, above 500 km s^{-1} , should be mostly composed of stars accelerated by the Milky Way Galactic center. As most of our stars have total velocities below 500 km s^{-1} it is possible that orbital calculations including the Magellanic Clouds potential could provide valuable additional information.

At least eight, out of our 15 targets, have chemical abundances and/or orbital parameters that diverge from the typical Milky Way. We identify those stars in Table 3 (identified by a c at the External ID field). At this point it is not possible to say with certainty that all our targets are accreted stars. However, based on the fact that at least 50% of our targets show evidence of being accreted we conclude that it is likely that the majority of the extreme-velocity stars are accreted.

5.2. The Acceleration Mechanism

The Hills mechanism (Hills 1988, 1991, 1992) accelerates stars via three body interactions between two binary stars and a massive black hole. It is understood that this mechanism would be prevalent in Milky Way stars that were formed in the bulge and then accelerated after interacting with Sagittarius A* (Sag. A*). In this scenario the stars can be accelerated up to $\sim 4000 \text{ km s}^{-1}$. An example of such an occurrence is S5-HVS 1, the 1700 km s^{-1} unbound star. Its orbit is indicative of interaction with Sag. A* (Koposov et al. 2020; Irrgang et al. 2021). Though the Hills mechanism does accelerate stars at low velocities as well, the stars in our sample are not compatible with the Hills mechanism. They are

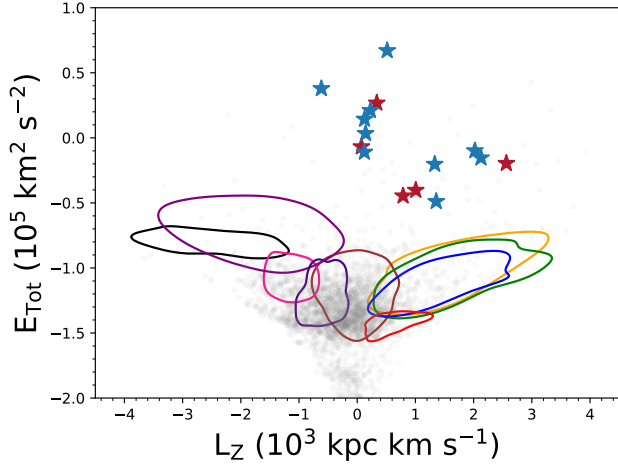


Figure 5. Total energy as a function of angular momentum. We separate our stars in two groups. In blue are our stars with $[\text{Mg}/\text{Fe}]_{\text{i}} > 0.2$ (more likely to be extragalactic) and in red stars with $[\text{Mg}/\text{Fe}]_{\text{i}} < 0.2$. The background gray data are galactic halo stars from (Naidu et al. 2021, private com). The colored ellipses are the substructures identified in Naidu et al. (2020). We include Arjuna, Cetus, GSE, Helmi, Itoi, Sequoia, Sgr., Thamnos, and Wukong (orange, black, brown, deep pink, green, blue, purple, red and indigo, respectively).

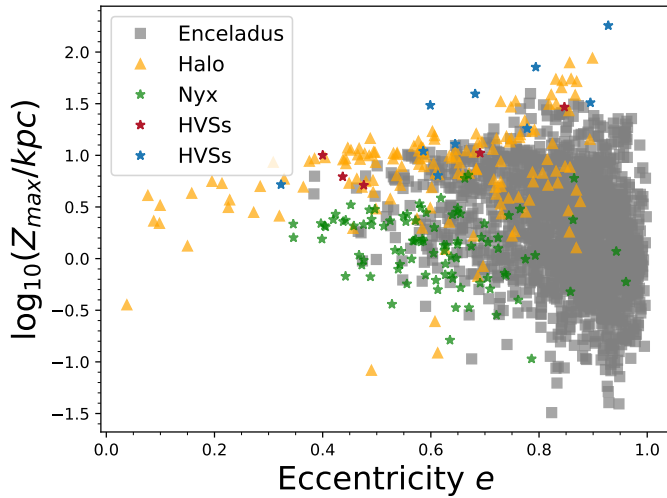


Figure 6. Distance from the Galactic Plane as a function of eccentricity. Orange triangles are stars from the Galactic Halo, gray squares are Enceladus stars, and green stars are from the Nyx stream (Necib et al. 2020). We separate our stars in two groups. In blue are our stars with $[\text{Mg}/\text{Fe}]_{\text{i}} > 0.2$ (more likely to be extragalactic) and in red stars with $[\text{Mg}/\text{Fe}]_{\text{i}} < 0.2$. Notice how all the stars with deviating eccentricity have low $[\text{Mg}/\text{Fe}]$ abundance.

neither travelling at the unique high velocities only produced by this mechanism, nor have chemical abundances consistent with the bulge (Figures 1 to 4). Besides, the pericenters of the stars in our sample are too large to be consistent with ejection by the Hills mechanism (the pericenters of our targets vary from $R_{\text{peri}} = 4.98$ kpc to $R_{\text{peri}} = 8.55$ kpc).

We also do not see chemical evidence that these stars were stripped from globular clusters. The stars do not show the anti-correlations observed for globular cluster stars (e.g. Mg-Al). This leaves us with two main possibilities: ejection from the LMC or tidal debris from disrupted dwarf galaxies. Even though we did not include the Magellanic Clouds potential in our orbital calculation, we see more than one possible cluster in orbital parameters among our stars, which is indicative of more than one origin. They do have high total energies, expected given their velocities, but their other orbital (and chemical) parameters vary considerably, thus indicating that they do not necessarily share the same origin.

Their chemistry does not point to the LMC either. As recently showed by Reggiani et al. (2021) Magellanic Clouds stars are r-process enhanced, and our targets do not show any clear level of r-process enhancement. Though our most metal-rich star have α -abundances that are consistent with the Magellanic Cloud, its apocenter is not large enough (31 kpc). It is also important to remark that most of our targets have metallicities lower than $[\text{Fe}/\text{H}] \leq -1.5$, a metallicity region that has not been thoroughly studied for the Magellanic Clouds, making any chemical comparison difficult (e.g. Nidever et al. 2020; Reggiani et al. 2021). Additional chemical abundances of Magellanic Clouds stars with $[\text{Fe}/\text{H}] \lesssim -1.5$ could provide further evidence, but with the data at hand it is not possible to confirm these stars are LMC runaways.

An alternative mechanism for accelerating stars into extreme velocities has been proposed by Abadi et al. (2009). They argued that the known population of HVSSs and their anisotropic distribution in the sky, and a preferred travel time, was inconsistent, at a population level, with the Hills mechanism scenario. They proposed that tidal disruptions of dwarf galaxies in the Galactic Potential could have accelerated at least a portion (the lower velocity portion) of the known HVSSs. Using a set of cosmological simulations they showed that a few million years after the disruption of a dwarf galaxy a tidal tail is formed, one in which stars are accelerated into extreme velocities, and can even become unbound from the main galaxy. Abadi et al. (2009) predicted that if this is a viable mechanism we would observe high-velocity stars preferably at low metallicities, including evolved

stars. They also predicted we could find a radial velocity angular gradient among the high-velocity stars. Another prediction is that this mechanism does not accelerate stars into velocities as high as those expected by the Hills mechanism. Therefore, though the young A and O stars, and other stars with velocities ~ 1000 km s $^{-1}$, are more likely to have been accelerated either by the Hills mechanism, or have been ejected from the LMC, the Abadi et al. (2009) provides an explanation for extreme-velocity stars such as those analyzed in this work.

As predicted by Abadi et al. (2009) our extreme-velocity stars are evolved metal-poor stars that, although fast, do not exceed the Galactic Potential escape velocity. The scenario outlined in Abadi et al. (2009) provide the most natural explanation for the conclusions about the origins of our targeted stars based on their chemical abundances, and different than the LMC scenario, it does not require a shared origin for most of our targets. It is also tempting to interpret the orbital clustering seen in Figure 5 as another prediction from their paper, though it is not, at this time, a statistically significant result.

6. CONCLUSION

We obtained high-resolution spectra of 15 low-mass hypervelocity stars candidates using either the MIKE spectrograph at the 6.5 meter Magellan telescope, or the ARCES spectrograph at the 3.5 meter Apache point Observatory telescope. We confirmed the radial velocities from Gaia DR2 and did not find signs of RV variability in these stars. The total velocities calculated using Gaia EDR3 astrometry and the inferred radial velocities confirm previous Gaia DR2 findings that they are bound to the Galactic potential and are not as fast as expected for classical hypervelocity stars.

The chemical patterns of the metal-rich end of our sample stars are consistent with that of extragalactic stars, with sub-solar α -abundances and supersolar neutron-capture abundances, and the iron-peak elements indicate sub-Chandrasekhar mass type Ia enrichment. Our orbital analysis is consistent with the chemical findings and our targets are not part of any Galactic substructure, although that is a biased result, as the very goal of the study is to study high velocity stars.

Our analysis of these extreme-velocity stars indicate that they are likely the tidal debris from disrupted dwarf galaxies accreted by the Milky Way, accelerated by the disruption of their host galaxy by the Galactic Potential (Abadi et al. 2009).

With the increasing identification of HVSS candidates, follow-up studies with larger samples will help us continue to determine the acceleration mechanism(s) mainly responsible for the fast tail of the Milky Way stellar velocity distribution. In particular, the upcoming Gaia DR3 updated radial velocities, along with the precise astrometric solutions, for millions of stars will allow us to identify both these extreme-velocity stars, and bona-fide hypervelocity stars. With a large enough sample we will be able to confirm/falsefy the Abadi et al. (2009) predictions based on orbital parameters and clustering information. A chemical analysis of additional candidates will provide further information about the stellar origins. Therefore, we strongly encourage a continued chemical characterization of these stars, in order to provide us with the information to characterize their acceleration mechanism(s) in a population level.

ACKNOWLEDGMENTS

We thank the referee for the careful analysis of our manuscript and the suggestions that helped us improve our study. We thank Ana Bonaca and Rohan Naidu for the valuable discussion on the paper and for kindly providing us with the orbital comparison data used in this study. HR acknowledges support from a Carnegie Fellowship. KH & TN acknowledge support from the National Science Foundation grant AST-1907417 and AST-2108736. KH is partially supported through the Wootton Center for Astrophysical Plasma Properties funded under the United States Department of Energy collaborative agreement. JYG acknowledges support from CNPq (166042/2020-0). This work was partially performed at the Aspen Center for Physics, which is supported by National Science Foundation grant PHY-1607611. This paper includes data gathered with the 6.5-meter Magellan Telescopes located at Las Campanas Observatory, Chile. This paper is partially based on observations obtained with the Apache Point Observatory 3.5-meter telescope, which is owned and operated by the Astrophysical Research Consortium. This work has made use of data from the European Space Agency (ESA) mission *Gaia* (<https://www.cosmos.esa.int/gaia>), processed by the *Gaia* Data Processing and Analysis Consortium (DPAC, <https://www.cosmos.esa.int/web/gaia/dpac/consortium>). Funding for the DPAC has been provided by national institutions, in particular the institutions participating in the *Gaia* Multilateral Agreement. This publication makes use of data products from the Wide-field Infrared Survey Explorer, which is a joint project of the University of California, Los Angeles, and the Jet Propulsion Laboratory/California Institute of Technology, and

NEOWISE, which is a project of the Jet Propulsion Laboratory/California Institute of Technology. WISE and NEOWISE are funded by the National Aeronautics and Space Administration. This publication makes use of data products from the Two Micron All Sky Survey, which is a joint project of the University of Massachusetts and the Infrared Processing and Analysis Center/California Institute of Technology, funded by the National Aeronautics and Space Administration and the National Science Foundation. This research has made use of the SkyMapper survey data release 2. The national facility capability for SkyMapper has been funded through ARC LIEF grant LE130100104 from the Australian Research Council, awarded to the University of Sydney, the Australian National University, Swinburne University of Technology, the University of Queensland, the University of Western Australia, the University of Melbourne, Curtin University of Technology, Monash University and the Australian Astronomical Observatory. SkyMapper is owned and operated by The Australian National University's Research School of Astronomy and Astrophysics. The survey data were processed and provided by the SkyMapper Team at ANU. The SkyMapper node of the All-Sky Virtual Observatory (ASVO) is hosted at the National Computational Infrastructure (NCI). Development and support of the SkyMapper node of the ASVO has been funded in part by Astronomy Australia Limited (AAL) and the Australian Government through the Commonwealth's Education Investment Fund (EIF) and National Collaborative Research Infrastructure Strategy (NCRIS), particularly the National eResearch Collaboration Tools and Resources (NeCTAR) and the Australian National

Data Service Projects (ANDS). This research has made use of NASA/IPAC Infrared Science Archive, which is funded by the National Aeronautics and Space Administration and operated by the California Institute of Technology (Skrutskie, M. F.; Cutri, R. M.; Stiening, R.; Weinberg, M. D.; Schneider, S.; Carpenter, J. M.; Beichman, C.; Capps, R.; Chester, T.; Elias, J.; Huchra, J.; Liebert, J.; Lonsdale, C.; Monet, D. G.; Price, S.; Seitzer, P.; Jarrett, T.; Kirkpatrick, J. D.; Gizis, J. E.; Howard, E.; Evans, T.; Fowler, J.; Fullmer, L.; Hurt, R.; Light, R.; Kopan, E. L.; Marsh, K. A.; McCallon, H. L.; Tam, R.; Van Dyk, S.; Wheelock, S. 2019; Wright, Edward L.; Eisenhardt, Peter R. M.; Mainzer, Amy K.; Ressler, Michael E.; Cutri, Roc M.; Jarrett, Thomas; Kirkpatrick, J. Davy; Padgett, Deborah; McMillan, Robert S.; Skrutskie, Michael; Stanford, S. A.; Cohen, Martin; Walker, Russell G.; Mather, John C.; Leisawitz, David; Gautier, Thomas N., III; McLean, Ian; Benford, Dominic; Lonsdale, Carol J.; Blain, Andrew; Mendez, Bryan; Irace, William R.; Duval, Valerie; Liu, Fengchuan; Royer, Don; Heinrichsen, Ingolf; Howard, Joan; et al. 2019).

Software: `astropy` (Astropy Collaboration et al. 2013, 2018), `CarPy` (Kelson et al. 2000; Kelson 2003), `galpy` (Bovy 2015), `q2` (Ramírez et al. 2014), `isochrones` (Morton 2015), `numpy` (Harris et al. 2020), `MultiNest` (Feroz & Hobson 2008; Feroz et al. 2009, 2019), `pandas` (McKinney 2010; pandas Development Team 2020), `scipy` (Virtanen et al. 2020), `IRAF` (Tody 1986, 1993), `matplotlib` (Hunter 2007)

Facilities: ARC (ARCES), Magellan:Clay (MIKE), CDS, Gaia, IRSA, Skymapper, CTIO:2MASS, WISE

REFERENCES

- Abadi, M. G., Navarro, J. F., & Steinmetz, M. 2009, *ApJL*, 691, L63, doi: [10.1088/0004-637X/691/2/L63](https://doi.org/10.1088/0004-637X/691/2/L63)
- Alonso, A., Arribas, S., & Martínez-Roger, C. 1999, *A&AS*, 140, 261, doi: [10.1051/aas:1999521](https://doi.org/10.1051/aas:1999521)
- Amarsi, A. M., Lind, K., Osorio, Y., et al. 2020, *A&A*, 642, A62, doi: [10.1051/0004-6361/202038650](https://doi.org/10.1051/0004-6361/202038650)
- Astropy Collaboration, Robitaille, T. P., Tollerud, E. J., et al. 2013, *A&A*, 558, A33, doi: [10.1051/0004-6361/201322068](https://doi.org/10.1051/0004-6361/201322068)
- Astropy Collaboration, Price-Whelan, A. M., Sipőcz, B. M., et al. 2018, *AJ*, 156, 123, doi: [10.3847/1538-3881/aabc4f](https://doi.org/10.3847/1538-3881/aabc4f)
- Bailer-Jones, C. A. L., Rybizki, J., Fouesneau, M., Demleitner, M., & Andrae, R. 2021, *AJ*, 161, 147, doi: [10.3847/1538-3881/abd806](https://doi.org/10.3847/1538-3881/abd806)
- Bensby, T., Feltzing, S., Johnson, J. A., et al. 2010, *A&A*, 512, A41, doi: [10.1051/0004-6361/200913744](https://doi.org/10.1051/0004-6361/200913744)
- Bernstein, R., Shectman, S. A., Gunnels, S. M., Mochnacki, S., & Athey, A. E. 2003, in *Society of Photo-Optical Instrumentation Engineers (SPIE) Conference Series*, Vol. 4841, Proc. SPIE, ed. M. Iye & A. F. M. Moorwood, 1694–1704, doi: [10.1117/12.461502](https://doi.org/10.1117/12.461502)
- Blaauw, A. 1961, *BAN*, 15, 265
- Blanco-Cuaresma, S. 2019, *MNRAS*, 486, 2075, doi: [10.1093/mnras/stz549](https://doi.org/10.1093/mnras/stz549)
- Blanco-Cuaresma, S., Soubiran, C., Heiter, U., & Jofré, P. 2014, *A&A*, 569, A111, doi: [10.1051/0004-6361/201423945](https://doi.org/10.1051/0004-6361/201423945)
- Bland-Hawthorn, J., & Gerhard, O. 2016, *ARA&A*, 54, 529, doi: [10.1146/annurev-astro-081915-023441](https://doi.org/10.1146/annurev-astro-081915-023441)
- Boubert, D., & Evans, N. W. 2016, *ApJL*, 825, L6, doi: [10.3847/2041-8205/825/1/L6](https://doi.org/10.3847/2041-8205/825/1/L6)

- Boubert, D., Guillochon, J., Hawkins, K., et al. 2018, *MNRAS*, 479, 2789, doi: [10.1093/mnras/sty1601](https://doi.org/10.1093/mnras/sty1601)
- Bovy, J. 2015, *ApJS*, 216, 29, doi: [10.1088/0067-0049/216/2/29](https://doi.org/10.1088/0067-0049/216/2/29)
- Brahm, R., Jordán, A., & Espinoza, N. 2017, *PASP*, 129, 034002, doi: [10.1088/1538-3873/aa5455](https://doi.org/10.1088/1538-3873/aa5455)
- Bromley, B. C., Kenyon, S. J., Brown, W. R., & Geller, M. J. 2009, *ApJ*, 706, 925, doi: [10.1088/0004-637X/706/2/925](https://doi.org/10.1088/0004-637X/706/2/925)
- . 2018, *ApJ*, 868, 25, doi: [10.3847/1538-4357/aae83e](https://doi.org/10.3847/1538-4357/aae83e)
- Brown, W. R. 2015, *ARA&A*, 53, 15, doi: [10.1146/annurev-astro-082214-122230](https://doi.org/10.1146/annurev-astro-082214-122230)
- Brown, W. R., Geller, M. J., Kenyon, S. J., & Kurtz, M. J. 2005, *ApJL*, 622, L33, doi: [10.1086/429378](https://doi.org/10.1086/429378)
- Buchner, J., Georgakakis, A., Nandra, K., et al. 2014, *A&A*, 564, A125, doi: [10.1051/0004-6361/201322971](https://doi.org/10.1051/0004-6361/201322971)
- Casey, A. R., Hawkins, K., Hogg, D. W., et al. 2017, *ApJ*, 840, 59, doi: [10.3847/1538-4357/aa69c2](https://doi.org/10.3847/1538-4357/aa69c2)
- Castelli, F., & Kurucz, R. L. 2004, *arXiv Astrophysics e-prints*
- Cayrel, R., Depagne, E., Spite, M., et al. 2004, *A&A*, 416, 1117, doi: [10.1051/0004-6361:20034074](https://doi.org/10.1051/0004-6361:20034074)
- Choi, J., Dotter, A., Conroy, C., et al. 2016, *ApJ*, 823, 102, doi: [10.3847/0004-637X/823/2/102](https://doi.org/10.3847/0004-637X/823/2/102)
- Clayton, D. 2007, *Handbook of Isotopes in the Cosmos*
- de los Reyes, M. A. C., Kirby, E. N., Seitzzahl, I. R., & Shen, K. J. 2020, *ApJ*, 891, 85, doi: [10.3847/1538-4357/ab736f](https://doi.org/10.3847/1538-4357/ab736f)
- Dotter, A. 2016, *ApJS*, 222, 8, doi: [10.3847/0067-0049/222/1/8](https://doi.org/10.3847/0067-0049/222/1/8)
- Erkal, D., Boubert, D., Gualandris, A., Evans, N. W., & Antonini, F. 2019, *MNRAS*, 483, 2007, doi: [10.1093/mnras/sty2674](https://doi.org/10.1093/mnras/sty2674)
- Evans, D. W., Riello, M., De Angeli, F., et al. 2018, *A&A*, 616, A4, doi: [10.1051/0004-6361/201832756](https://doi.org/10.1051/0004-6361/201832756)
- Evans, F. A., Marchetti, T., Rossi, E. M., Baggen, J. F. W., & Bloot, S. 2021, *arXiv e-prints*, arXiv:2108.01100. <https://arxiv.org/abs/2108.01100>
- Feroz, F., & Hobson, M. P. 2008, *MNRAS*, 384, 449, doi: [10.1111/j.1365-2966.2007.12353.x](https://doi.org/10.1111/j.1365-2966.2007.12353.x)
- Feroz, F., Hobson, M. P., & Bridges, M. 2009, *MNRAS*, 398, 1601, doi: [10.1111/j.1365-2966.2009.14548.x](https://doi.org/10.1111/j.1365-2966.2009.14548.x)
- Feroz, F., Hobson, M. P., Cameron, E., & Pettitt, A. N. 2019, *The Open Journal of Astrophysics*, 2, 10, doi: [10.21105/astro.1306.2144](https://doi.org/10.21105/astro.1306.2144)
- Frebel, A., Christlieb, N., Norris, J. E., et al. 2007, *ApJL*, 660, L117, doi: [10.1086/518122](https://doi.org/10.1086/518122)
- Gaia Collaboration, Brown, A. G. A., Vallenari, A., et al. 2020, *arXiv e-prints*, arXiv:2012.01533. <https://arxiv.org/abs/2012.01533>
- Gaia Collaboration, Prusti, T., de Bruijne, J. H. J., et al. 2016, *A&A*, 595, A1, doi: [10.1051/0004-6361/201629272](https://doi.org/10.1051/0004-6361/201629272)
- Gaia Collaboration, Brown, A. G. A., Vallenari, A., et al. 2018, *A&A*, 616, A1, doi: [10.1051/0004-6361/201833051](https://doi.org/10.1051/0004-6361/201833051)
- Geisler, D., Smith, V. V., Wallerstein, G., Gonzalez, G., & Charbonnel, C. 2005, *AJ*, 129, 1428, doi: [10.1086/427540](https://doi.org/10.1086/427540)
- Gravity Collaboration, Abuter, R., Amorim, A., et al. 2018, *A&A*, 615, L15, doi: [10.1051/0004-6361/201833718](https://doi.org/10.1051/0004-6361/201833718)
- Green, G. M., Schlafly, E., Zucker, C., Speagle, J. S., & Finkbeiner, D. 2019, *ApJ*, 887, 93, doi: [10.3847/1538-4357/ab5362](https://doi.org/10.3847/1538-4357/ab5362)
- Hansen, C. J., Bergemann, M., Cescutti, G., et al. 2013, *A&A*, 551, A57, doi: [10.1051/0004-6361/201220584](https://doi.org/10.1051/0004-6361/201220584)
- Harris, C. R., Millman, K. J., van der Walt, S. J., et al. 2020, *Nature*, 585, 357, doi: [10.1038/s41586-020-2649-2](https://doi.org/10.1038/s41586-020-2649-2)
- Hattori, K., Valluri, M., Bell, E. F., & Roederer, I. U. 2018a, *ApJ*, 866, 121, doi: [10.3847/1538-4357/aadee5](https://doi.org/10.3847/1538-4357/aadee5)
- Hattori, K., Valluri, M., & Castro, N. 2018b, *ApJ*, 869, 33, doi: [10.3847/1538-4357/aaed22](https://doi.org/10.3847/1538-4357/aaed22)
- Hawkins, K., & Wyse, R. F. G. 2018, *MNRAS*, 481, 1028, doi: [10.1093/mnras/sty2282](https://doi.org/10.1093/mnras/sty2282)
- Hayes, C. R., Majewski, S. R., Shetrone, M., et al. 2018, *ApJ*, 852, 49, doi: [10.3847/1538-4357/aa9ccc](https://doi.org/10.3847/1538-4357/aa9ccc)
- Herzog-Arbeitman, J., Lisanti, M., & Necib, L. 2018, *JCAP*, 2018, 052, doi: [10.1088/1475-7516/2018/04/052](https://doi.org/10.1088/1475-7516/2018/04/052)
- Hills, J. G. 1988, *Nature*, 331, 687, doi: [10.1038/331687a0](https://doi.org/10.1038/331687a0)
- . 1991, *AJ*, 102, 704, doi: [10.1086/115905](https://doi.org/10.1086/115905)
- . 1992, *AJ*, 103, 1955, doi: [10.1086/116204](https://doi.org/10.1086/116204)
- Hunter, J. D. 2007, *Computing in Science & Engineering*, 9, 90, doi: [10.1109/MCSE.2007.55](https://doi.org/10.1109/MCSE.2007.55)
- Irrgang, A., Dimpel, M., Heber, U., & Raddi, R. 2021, *A&A*, 646, L4, doi: [10.1051/0004-6361/202040178](https://doi.org/10.1051/0004-6361/202040178)
- Jacobson, H. R., Keller, S., Frebel, A., et al. 2015, *ApJ*, 807, 171, doi: [10.1088/0004-637X/807/2/171](https://doi.org/10.1088/0004-637X/807/2/171)
- Ji, A. P., Frebel, A., Chiti, A., & Simon, J. D. 2016, *Nature*, 531, 610, doi: [10.1038/nature17425](https://doi.org/10.1038/nature17425)
- Ji, A. P., Li, T. S., Hansen, T. T., et al. 2020, *AJ*, 160, 181, doi: [10.3847/1538-3881/abacb6](https://doi.org/10.3847/1538-3881/abacb6)
- Jurić, M., Ivezić, Ž., Brooks, A., et al. 2008, *ApJ*, 673, 864, doi: [10.1086/523619](https://doi.org/10.1086/523619)
- Kelson, D. D. 2003, *PASP*, 115, 688, doi: [10.1086/375502](https://doi.org/10.1086/375502)
- Kelson, D. D., Illingworth, G. D., van Dokkum, P. G., & Franx, M. 2000, *ApJ*, 531, 159, doi: [10.1086/308445](https://doi.org/10.1086/308445)
- Kelson, D. D., Williams, R. J., Dressler, A., et al. 2014, *ApJ*, 783, 110, doi: [10.1088/0004-637X/783/2/110](https://doi.org/10.1088/0004-637X/783/2/110)
- Kirby, E. N., Guhathakurta, P., Bolte, M., Sneden, C., & Geha, M. C. 2009, *ApJ*, 705, 328, doi: [10.1088/0004-637X/705/1/328](https://doi.org/10.1088/0004-637X/705/1/328)

- Klose, J. Z., Fuhr, J. R., & Wiese, W. L. 2002, *Journal of Physical and Chemical Reference Data*, 31, 217, doi: [10.1063/1.1448482](https://doi.org/10.1063/1.1448482)
- Kobayashi, C., Karakas, A. I., & Lugaro, M. 2020a, *ApJ*, 900, 179, doi: [10.3847/1538-4357/abae65](https://doi.org/10.3847/1538-4357/abae65)
- Kobayashi, C., Leung, S.-C., & Nomoto, K. 2020b, *ApJ*, 895, 138, doi: [10.3847/1538-4357/ab8e44](https://doi.org/10.3847/1538-4357/ab8e44)
- Koposov, S. E., Boubert, D., Li, T. S., et al. 2020, *MNRAS*, 491, 2465, doi: [10.1093/mnras/stz3081](https://doi.org/10.1093/mnras/stz3081)
- Kunder, A., Kordopatis, G., Steinmetz, M., et al. 2017, *AJ*, 153, 75, doi: [10.3847/1538-3881/153/2/75](https://doi.org/10.3847/1538-3881/153/2/75)
- Leonard, P. J. T. 1991, *AJ*, 101, 562, doi: [10.1086/115704](https://doi.org/10.1086/115704)
- Letarte, B., Hill, V., Tolstoy, E., et al. 2010, *A&A*, 523, A17, doi: [10.1051/0004-6361/200913413](https://doi.org/10.1051/0004-6361/200913413)
- Lind, K., Asplund, M., Barklem, P. S., & Belyaev, A. K. 2011, *A&A*, 528, A103, doi: [10.1051/0004-6361/201016095](https://doi.org/10.1051/0004-6361/201016095)
- Lindgren, L., Bastian, U., Biermann, M., et al. 2020, arXiv e-prints, arXiv:2012.01742. <https://arxiv.org/abs/2012.01742>
- Mainzer, A., Grav, T., Bauer, J., et al. 2011, *ApJ*, 743, 156, doi: [10.1088/0004-637X/743/2/156](https://doi.org/10.1088/0004-637X/743/2/156)
- Marchetti, T., Contigiani, O., Rossi, E. M., et al. 2018a, *MNRAS*, 476, 4697, doi: [10.1093/mnras/sty579](https://doi.org/10.1093/mnras/sty579)
- Marchetti, T., Rossi, E. M., Kordopatis, G., et al. 2018b, in *Astrometry and Astrophysics in the Gaia Sky*, ed. A. Recio-Blanco, P. de Laverny, A. G. A. Brown, & T. Prusti, Vol. 330, 181–184, doi: [10.1017/S1743921317005671](https://doi.org/10.1017/S1743921317005671)
- Matteucci, F., & Brocato, E. 1990, *ApJ*, 365, 539, doi: [10.1086/169508](https://doi.org/10.1086/169508)
- McKinney, W. 2010, in *Proceedings of the 9th Python in Science Conference*, ed. Stéfan van der Walt & Jarrod Millman, 56 – 61, doi: [10.25080/Majora-92bf1922-00a](https://doi.org/10.25080/Majora-92bf1922-00a)
- McWilliam, A. 1998, *AJ*, 115, 1640, doi: [10.1086/300289](https://doi.org/10.1086/300289)
- Miyamoto, M., & Nagai, R. 1975, *PASJ*, 27, 533
- Monaco, L., Bellazzini, M., Bonifacio, P., et al. 2005, *A&A*, 441, 141, doi: [10.1051/0004-6361:20053333](https://doi.org/10.1051/0004-6361:20053333)
- Morton, T. D. 2015, *isochrones: Stellar model grid package*. <http://ascl.net/1503.010>
- Naidu, R. P., Conroy, C., Bonaca, A., et al. 2020, *ApJ*, 901, 48, doi: [10.3847/1538-4357/abaef4](https://doi.org/10.3847/1538-4357/abaef4)
- Naidu, R. P., Ji, A. P., Conroy, C., et al. 2021, arXiv e-prints, arXiv:2110.14652. <https://arxiv.org/abs/2110.14652>
- Navarro, J. F., Frenk, C. S., & White, S. D. M. 1996, *ApJ*, 462, 563, doi: [10.1086/177173](https://doi.org/10.1086/177173)
- Necib, L., Ostdiek, B., Lisanti, M., et al. 2020, *ApJ*, 903, 25, doi: [10.3847/1538-4357/abb814](https://doi.org/10.3847/1538-4357/abb814)
- Ness, M., Hogg, D. W., Rix, H. W., Ho, A. Y. Q., & Zasowski, G. 2015, *ApJ*, 808, 16, doi: [10.1088/0004-637X/808/1/16](https://doi.org/10.1088/0004-637X/808/1/16)
- Ness, M., Hogg, D. W., Rix, H. W., et al. 2016, *ApJ*, 823, 114, doi: [10.3847/0004-637X/823/2/114](https://doi.org/10.3847/0004-637X/823/2/114)
- Nidever, D. L., Hasselquist, S., Hayes, C. R., et al. 2020, *ApJ*, 895, 88, doi: [10.3847/1538-4357/ab7305](https://doi.org/10.3847/1538-4357/ab7305)
- Nissen, P. E., & Schuster, W. J. 2010, *A&A*, 511, L10, doi: [10.1051/0004-6361/200913877](https://doi.org/10.1051/0004-6361/200913877)
- Nordlander, T., & Lind, K. 2017, *A&A*, 607, A75, doi: [10.1051/0004-6361/201730427](https://doi.org/10.1051/0004-6361/201730427)
- pandas Development Team. 2020, *pandas-dev/pandas: Pandas, latest*, Zenodo, doi: [10.5281/zenodo.3509134](https://doi.org/10.5281/zenodo.3509134)
- Paxton, B., Bildsten, L., Dotter, A., et al. 2011, *ApJS*, 192, 3, doi: [10.1088/0067-0049/192/1/3](https://doi.org/10.1088/0067-0049/192/1/3)
- Paxton, B., Cantiello, M., Arras, P., et al. 2013, *ApJS*, 208, 4, doi: [10.1088/0067-0049/208/1/4](https://doi.org/10.1088/0067-0049/208/1/4)
- Paxton, B., Marchant, P., Schwab, J., et al. 2015, *ApJS*, 220, 15, doi: [10.1088/0067-0049/220/1/15](https://doi.org/10.1088/0067-0049/220/1/15)
- Placco, V. M., Sneden, C., Roederer, I. U., et al. 2021, *Research Notes of the American Astronomical Society*, 5, 92, doi: [10.3847/2515-5172/abf651](https://doi.org/10.3847/2515-5172/abf651)
- Poveda, A., Ruiz, J., & Allen, C. 1967, *Boletín de los Observatorios Tonantzintla y Tacubaya*, 4, 86
- Prantzos, N., Abia, C., Limongi, M., Chieffi, A., & Cristallo, S. 2018, *MNRAS*, 476, 3432, doi: [10.1093/mnras/sty316](https://doi.org/10.1093/mnras/sty316)
- Ramírez, I., Meléndez, J., Bean, J., et al. 2014, *A&A*, 572, A48, doi: [10.1051/0004-6361/201424244](https://doi.org/10.1051/0004-6361/201424244)
- Reggiani, H., & Meléndez, J. 2018, *MNRAS*, 475, 3502, doi: [10.1093/mnras/sty104](https://doi.org/10.1093/mnras/sty104)
- Reggiani, H., Meléndez, J., Kobayashi, C., Karakas, A., & Placco, V. 2017, *A&A*, 608, A46, doi: [10.1051/0004-6361/201730750](https://doi.org/10.1051/0004-6361/201730750)
- Reggiani, H., Schlaufman, K. C., Casey, A. R., & Ji, A. P. 2020, *AJ*, 160, 173, doi: [10.3847/1538-3881/aba948](https://doi.org/10.3847/1538-3881/aba948)
- Reggiani, H., Schlaufman, K. C., Casey, A. R., Simon, J. D., & Ji, A. P. 2021, arXiv e-prints, arXiv:2108.10880. <https://arxiv.org/abs/2108.10880>
- Reggiani, H., Schlaufman, K. C., Healy, B. F., Lothringer, J. D., & Sing, D. K. 2022, arXiv e-prints, arXiv:2201.08508. <https://arxiv.org/abs/2201.08508>
- Reggiani, H., Amarsi, A. M., Lind, K., et al. 2019, *A&A*, 627, A177, doi: [10.1051/0004-6361/201935156](https://doi.org/10.1051/0004-6361/201935156)
- Sakari, C. M., Placco, V. M., Farrell, E. M., et al. 2018, *ApJ*, 868, 110, doi: [10.3847/1538-4357/aae9df](https://doi.org/10.3847/1538-4357/aae9df)
- Sanders, J. L., Belokurov, V., & Man, K. T. F. 2021, *MNRAS*, 506, 4321, doi: [10.1093/mnras/stab1951](https://doi.org/10.1093/mnras/stab1951)

- Shectman, S. A., & Johns, M. 2003, in Society of Photo-Optical Instrumentation Engineers (SPIE) Conference Series, Vol. 4837, Proc. SPIE, ed. J. M. Oschmann & L. M. Stepp, 910–918, doi: [10.1117/12.457909](https://doi.org/10.1117/12.457909)
- Shen, K. J., Boubert, D., Gänsicke, B. T., et al. 2018, ApJ, 865, 15, doi: [10.3847/1538-4357/aad55b](https://doi.org/10.3847/1538-4357/aad55b)
- Shetrone, M., Venn, K. A., Tolstoy, E., et al. 2003, AJ, 125, 684, doi: [10.1086/345966](https://doi.org/10.1086/345966)
- Skrutskie, M. F., Cutri, R. M., Stiening, R., et al. 2006, AJ, 131, 1163, doi: [10.1086/498708](https://doi.org/10.1086/498708)
- Skrutskie, M. F.; Cutri, R. M.; Stiening, R.; Weinberg, M. D.; Schneider, S.; Carpenter, J. M.; Beichman, C.; Capps, R.; Chester, T.; Elias, J.; Huchra, J.; Liebert, J.; Lonsdale, C.; Monet, D. G.; Price, S.; Seitzer, P.; Jarrett, T.; Kirkpatrick, J. D.; Gizis, J. E.; Howard, E.; Evans, T.; Fowler, J.; Fullmer, L.; Hurt, R.; Light, R.; Kopan, E. L.; Marsh, K. A.; McCallon, H. L.; Tam, R.; Van Dyk, S.; Wheelock, S. 2019, 2MASS All-Sky Point Source Catalog, IPAC, doi: [10.26131/IRSA2](https://doi.org/10.26131/IRSA2)
- Snedden, C., Lawler, J. E., Cowan, J. J., Ivans, I. I., & Den Hartog, E. A. 2009, ApJS, 182, 80, doi: [10.1088/0067-0049/182/1/80](https://doi.org/10.1088/0067-0049/182/1/80)
- Snedden, C., Lawler, J. E., den Hartog, E. A., & Wood, M. E. 2016, IAU Focus Meeting, 29A, 287, doi: [10.1017/S1743921316003069](https://doi.org/10.1017/S1743921316003069)
- Snedden, C. A. 1973, PhD thesis, THE UNIVERSITY OF TEXAS AT AUSTIN.
- Suda, T., Hidaka, J., Aoki, W., et al. 2017, PASJ, 69, 76, doi: [10.1093/pasj/psx059](https://doi.org/10.1093/pasj/psx059)
- Tinsley, B. M. 1979, ApJ, 229, 1046, doi: [10.1086/157039](https://doi.org/10.1086/157039)
- Tody, D. 1986, Society of Photo-Optical Instrumentation Engineers (SPIE) Conference Series, Vol. 627, The IRAF Data Reduction and Analysis System, ed. D. L. Crawford, 733, doi: [10.1117/12.968154](https://doi.org/10.1117/12.968154)
- . 1993, Astronomical Society of the Pacific Conference Series, Vol. 52, IRAF in the Nineties, ed. R. J. Hanisch, R. J. V. Brissenden, & J. Barnes, 173
- Virtanen, P., Gommers, R., Oliphant, T. E., et al. 2020, Nature Methods, 17, 261, doi: [10.1038/s41592-019-0686-2](https://doi.org/10.1038/s41592-019-0686-2)
- Wolf, C., Onken, C. A., Luvaul, L. C., et al. 2018, PASA, 35, e010, doi: [10.1017/pasa.2018.5](https://doi.org/10.1017/pasa.2018.5)
- Wright, E. L., Eisenhardt, P. R. M., Mainzer, A. K., et al. 2010, AJ, 140, 1868, doi: [10.1088/0004-6256/140/6/1868](https://doi.org/10.1088/0004-6256/140/6/1868)
- Wright, Edward L.; Eisenhardt, Peter R. M.; Mainzer, Amy K.; Ressler, Michael E.; Cutri, Roc M.; Jarrett, Thomas; Kirkpatrick, J. Davy; Padgett, Deborah; McMillan, Robert S.; Skrutskie, Michael; Stanford, S. A.; Cohen, Martin; Walker, Russell G.; Mather, John C.; Leisawitz, David; Gautier, Thomas N., III; McLean, Ian; Benford, Dominic; Lonsdale, Carol J.; Blain, Andrew; Mendez, Bryan; Irace, William R.; Duval, Valerie; Liu, Fengchuan; Royer, Don; Heinrichsen, Ingolf; Howard, Joan; et al. 2019, AllWISE Source Catalog, IPAC, doi: [10.26131/IRSA1](https://doi.org/10.26131/IRSA1)
- Yu, Q., & Tremaine, S. 2003, ApJ, 599, 1129, doi: [10.1086/379546](https://doi.org/10.1086/379546)
- Zhao, G., Mashonkina, L., Yan, H. L., et al. 2016, ApJ, 833, 225, doi: [10.3847/1538-4357/833/2/225](https://doi.org/10.3847/1538-4357/833/2/225)

Table 2. Atomic data, Equivalent Widths and line Abundances. Full version online.

Gaia EDR3 Source ID	Wavelength (Å)	Species	Excitation Potential (eV)	$\log(gf)$	EW (mÅ)	$\log_{\epsilon}(X)$
3252546886080448384	5889.951	Na I	0.000	0.108	177.00	4.497
3252546886080448384	5895.924	Na I	0.000	-0.194	131.30	4.315
2629296824480015744	5682.633	Na I	2.102	-0.706	36.70	4.971
2629296824480015744	5688.203	Na I	2.104	-0.406	47.90	4.852
6505889848642319872	5682.633	Na I	2.102	-0.706	18.80	4.388
6505889848642319872	5688.203	Na I	2.104	-0.406	32.70	4.397
3252546886080448384	3986.753	Mg I	4.346	-1.060	38.40	5.770
3252546886080448384	4057.505	Mg I	4.346	-0.900	22.70	5.322
3252546886080448384	4167.271	Mg I	4.346	-0.745	60.30	5.796
3252546886080448384	4702.991	Mg I	4.346	-0.440	80.10	5.718
3252546886080448384	4283.011	Ca I	1.886	-0.224	61.40	4.616

NOTE—This table is published in its entirety in the machine-readable format. A portion is shown here for guidance regarding its form and content.

Table 3. Stellar Properties and Adopted Parameters

Property	2853089398265954432	330414789019026944	2260163008363761664	2233912206910720000	1765600930139450752	Units
Photometric Properties						
External ID	TYC 1732-2222-1 ^c	TYC 2319-713-1 ^c	ES26 ^c	ES10 ^c	TYC 1126-382-1	
Gaia EDR3 parallax	0.830 ± 0.053	0.496 ± 0.034	0.336 ± 0.012	0.354 ± 0.014	0.613 ± 0.022	mas
Gaia DR2 G	11.012 ± 0.002	11.664 ± 0.002	11.821 ± 0.002	12.959 ± 0.002	11.865 ± 0.002	Vega mag
Gaia DR2 BP	11.569 ± 0.002	12.150 ± 0.002	12.318 ± 0.002	13.391 ± 0.002	12.341 ± 0.002	Vega mag
Gaia DR2 RP	10.347 ± 0.002	11.021 ± 0.002	11.178 ± 0.002	12.351 ± 0.002	11.233 ± 0.002	Vega mag
SkyMapper <i>u</i>	AB mag
SkyMapper <i>v</i>	AB mag
SkyMapper <i>g</i>	AB mag
SkyMapper <i>r</i>	AB mag
SkyMapper <i>i</i>	AB mag
SkyMapper <i>z</i>	AB mag
2MASS <i>J</i>	9.499 ± 0.022	10.158 ± 0.020	10.332 ± 0.021	11.589 ± 0.024	10.419 ± 0.022	Vega mag
2MASS <i>H</i>	9.069 ± 0.022	9.708 ± 0.023	9.818 ± 0.017	11.164 ± 0.027	9.935 ± 0.023	Vega mag
2MASS <i>K</i>	8.923 ± 0.022	9.602 ± 0.021	9.740 ± 0.016	11.085 ± 0.021	9.836 ± 0.021	Vega mag
WISE W1	8.837 ± 0.022	9.510 ± 0.022	9.667 ± 0.023	11.019 ± 0.023	9.769 ± 0.023	Vega mag
WISE W2	8.896 ± 0.020	9.537 ± 0.020	9.692 ± 0.020	11.035 ± 0.020	9.782 ± 0.020	Vega mag
Stellar Properties						
Distance d_{iso}	1.2 ^{+0.1} _{-0.1}	2.0 ^{+0.1} _{-0.1}	2.8 ^{+0.1} _{-0.1}	2.8 ^{+0.1} _{-0.1}	1.6 ^{+0.1} _{-0.1}	kpc
Mass M_{\odot}	0.90 ^{+0.04} _{-0.04}	0.95 ^{+0.07} _{-0.07}	0.78 ^{+0.01} _{-0.01}	0.78 ^{+0.01} _{-0.01}	0.78 ^{+0.01} _{-0.01}	M_{\odot}
Extinction A_V	0.312 ^{+0.006} _{-0.012}	0.448 ^{+0.009} _{-0.016}	0.178 ^{+0.003} _{-0.003}	0.353 ^{+0.028} _{-0.039}	0.319 ^{+0.001} _{-0.002}	mag
Effective temperature T_{eff}	4887 ± 100	5204 ± 100	4927 ± 100	5378 ± 100	5146 ± 100	K
Surface gravity $\log g$	2.33 ± 0.15	2.23 ± 0.15	1.90 ± 0.15	2.48 ± 0.15	2.45 ± 0.15	cm s ⁻²
Metallicity [Fe/H]	-1.13 ± 0.27	-2.54 ± 0.27	-2.04 ± 0.37	-0.95 ± 0.23	-1.97 ± 0.28	
Microturbulence ξ	1.59 ± 0.10	1.62 ± 0.10	1.69 ± 0.10	1.56 ± 0.10	1.57 ± 0.10	km s ⁻¹
Orbital Properties						
Radial Velocity RV	-303.5 ± 2.0	-120.6 ± 1.5	14.6 ± 1.0	-343.9 ± 1.1	-271.8 ± 0.5	km s ⁻¹
Total Galactic velocity v	359.8 ^{+12.6} _{-12.2}	519.8 ^{+5.8} _{-9.4}	385.0 ^{+2.1} _{-4.3}	436.7 ^{+2.5} _{-4.3}	484.4 ^{+3.0} _{-5.5}	km s ⁻¹
Pericenter Rperi	7.88 ^{+2.86} _{-2.86}	9.58 ^{+0.03} _{-0.03}	8.41 ^{+8.31} _{-8.31}	8.55 ^{+0.01} _{-0.01}	7.75 ^{+0.01} _{-0.01}	kpc
Apocenter Rapo	31.14 ^{+4.26} _{-3.40}	257.91 ^{+10.35} _{-17.23}	44.40 ^{+1.46} _{-2.34}	74.57 ^{+3.09} _{-4.87}	140.62 ^{+7.20} _{-13.91}	kpc
Eccentricity e	0.61 ^{+0.05} _{-0.05}	0.93 ^{+0.01} _{-0.01}	0.68 ^{+0.11} _{-0.11}	0.79 ^{+0.01} _{-0.01}	0.90 ^{+0.01} _{-0.01}	
Maximum distance from Galactic plane z_{max}	6.38 ^{+1.52} _{-1.52}	180.59 ^{+17.37} _{-17.37}	39.32 ^{+3.72} _{-3.72}	71.49 ^{+3.97} _{-3.97}	32.36 ^{+3.25} _{-3.25}	kpc
Total orbital energy E_{tot}	-9893 ⁺⁴⁷²⁰ ₋₄₄₀₅	67044 ⁺³¹¹¹ ₋₄₉₇₆	3367 ⁺⁸⁷⁹ ₋₁₇₁₈	21039 ⁺¹¹³⁰ ₋₁₉₁₄	37869 ⁺¹⁴³³ ₋₂₆₄₂	km ² s ⁻²
Angular momentum L_Z	2021 ⁺⁷⁸ ₋₇₆	514 ⁺²² ₋₃₇	144 ⁺¹⁷ ₋₃₅	227 ⁺²³ ₋₂₃	-616 ⁺¹⁰ ₋₇	kpc km s ⁻¹
Property	3252546886080448384	5212110596595560192	5212817273334550016	3599974177996428032	6317828550897175936	Units
Photometric Properties						
External ID	ES1	ES8	ES5 ^c	TYC 4934-700-1	HE 1523-0901 ^c	
Gaia EDR3 parallax	1.321 ± 0.043	0.444 ± 0.009	0.357 ± 0.010	0.362 ± 0.017	0.328 ± 0.020	mas
Gaia DR2 G	12.073 ± 0.002	10.713 ± 0.002	10.895 ± 0.002	10.771 ± 0.002	10.744 ± 0.002	Vega mag
Gaia DR2 BP	12.391 ± 0.002	11.328 ± 0.002	11.655 ± 0.002	11.325 ± 0.002	11.391 ± 0.002	Vega mag
Gaia DR2 RP	11.584 ± 0.002	9.982 ± 0.002	10.069 ± 0.002	10.092 ± 0.002	9.992 ± 0.002	Vega mag
SkyMapper <i>u</i>	13.509 ± 0.012	13.494 ± 0.020	14.421 ± 0.012	13.409 ± 0.002	13.722 ± 0.007	AB mag
SkyMapper <i>v</i>	13.132 ± 0.011	12.931 ± 0.006	13.924 ± 0.007	12.726 ± 0.006	13.058 ± 0.005	AB mag
SkyMapper <i>g</i>	...	11.308 ± 0.006	11.678 ± 0.005	11.301 ± 0.007	11.394 ± 0.005	AB mag
SkyMapper <i>r</i>	...	10.750 ± 0.004	10.964 ± 0.006	10.810 ± 0.008	10.797 ± 0.005	AB mag

Table 3 continued

Table 3 (continued)

SkyMapper z	...	10.323 ± 0.004	10.420 ± 0.007	...	10.336 ± 0.007	AB mag
SkyMapper z	...	10.137 ± 0.004	10.178 ± 0.007	...	10.149 ± 0.011	AB mag
2MASS J	10.957 ± 0.024	9.000 ± 0.023	8.881 ± 0.024	9.238 ± 0.026	9.027 ± 0.028	Vega mag
2MASS H	10.635 ± 0.024	8.410 ± 0.031	8.199 ± 0.023	8.699 ± 0.055	8.421 ± 0.031	Vega mag
2MASS K	10.523 ± 0.021	8.289 ± 0.033	8.022 ± 0.017	8.551 ± 0.021	8.352 ± 0.027	Vega mag
WISE W1	10.521 ± 0.023	8.157 ± 0.023	7.930 ± 0.026	8.466 ± 0.022	8.200 ± 0.024	Vega mag
WISE W2	10.514 ± 0.020	8.191 ± 0.020	7.988 ± 0.020	8.497 ± 0.020	8.199 ± 0.021	Vega mag
Stellar Properties						
Distance d_{iso}	$0.8^{+0.1}_{-0.1}$	$2.2^{+0.1}_{-0.1}$	$2.7^{+0.1}_{-0.1}$	$2.6^{+0.1}_{-0.1}$	$2.9^{+0.1}_{-0.1}$	kpc
Mass M_{\odot}	$0.79^{+0.02}_{-0.01}$	$0.98^{+0.07}_{-0.05}$	$1.95^{+0.03}_{-0.02}$	$0.78^{+0.01}_{-0.01}$	$0.80^{+0.01}_{-0.01}$	M_{\odot}
Extinction A_V	$0.029^{+0.028}_{-0.018}$	$0.374^{+0.022}_{-0.017}$	$0.659^{+0.001}_{-0.001}$	$0.100^{+0.001}_{-0.001}$	$0.370^{+0.001}_{-0.001}$	mag
Effective temperature T_{eff}	5620 ± 100	4688 ± 100	4481 ± 100	4783 ± 100	4742 ± 100	K
Surface gravity $\log g$	3.45 ± 0.15	1.60 ± 0.15	1.61 ± 0.15	1.51 ± 0.15	1.29 ± 0.15	cm s^{-2}
Metallicity $[\text{Fe}/\text{H}]$	-1.90 ± 0.10	-1.56 ± 0.12	-0.84 ± 0.19	-2.33 ± 0.10	-2.65 ± 0.22	
Microturbulence ξ	1.34 ± 0.10	1.76 ± 0.10	1.76 ± 0.10	1.78 ± 0.10	1.83 ± 0.10	km s^{-1}
Orbital Properties						
Radial Velocity RV	1.7 ± 1.2	298.2 ± 1.5	159.9 ± 0.5	291.5 ± 0.9	-162.4 ± 1.5	km s^{-1}
Total Galactic velocity v	$326.2^{+5.9}_{-8.6}$	$460.2^{+3.2}_{-4.2}$	$367.5^{+0.2}_{-0.2}$	$327.2^{+0.5}_{-0.5}$	$287.0^{+0.6}_{-0.6}$	km s^{-1}
Pericenter R_{peri}	$4.98^{+0.44}_{-0.44}$	$7.75^{+0.01}_{-0.01}$	$7.82^{+0.01}_{-0.01}$	$8.45^{+0.01}_{-0.01}$	$5.34^{+0.08}_{-0.02}$	kpc
Apocenter R_{apo}	$23.30^{+0.58}_{-1.00}$	$93.90^{+4.70}_{-6.51}$	$31.18^{+0.06}_{-0.05}$	$21.56^{+0.04}_{-0.05}$	$10.43^{+0.04}_{-0.04}$	kpc
Eccentricity e	$0.65^{+0.09}_{-0.03}$	$0.85^{+0.01}_{-0.01}$	$0.60^{+0.01}_{-0.01}$	$0.44^{+0.01}_{-0.01}$	$0.32^{+0.01}_{-0.01}$	
Maximum distance from Galactic plane z_{max}	$12.85^{+0.24}_{-1.37}$	$29.34^{+1.44}_{-1.96}$	$30.52^{+0.08}_{-0.08}$	$6.21^{+0.03}_{-0.03}$	$5.21^{+0.07}_{-0.05}$	kpc
Total orbital energy E_{tot}	-20298^{+2015}_{-2849}	26766^{+1466}_{-1959}	-10979^{+99}_{-84}	-19605^{+168}_{-161}	-48894^{+162}_{-155}	$\text{km}^2 \text{ s}^{-2}$
Angular momentum L_Z	1331^{+69}_{-69}	336^{+12}_{-12}	123^{+7}_{-7}	2561^{+5}_{-4}	1356^{+1}_{-1}	kpc km s^{-1}
Property	6479574961975897856	6558932694746826240	2629296824480015744	6505889848642319872	6556192329517108352	Units
Photometric Properties						
External ID	TYC 8429-663-1	TYC 8443-1432-1 ^c	ES3 ^c	ES4	TYC 7509-604-1	
Gaia EDR3 parallax	0.304 ± 0.013	0.341 ± 0.018	1.522 ± 0.042	0.379 ± 0.019	0.253 ± 0.018	mas
Gaia DR2 G	10.583 ± 0.002	11.458 ± 0.002	11.365 ± 0.002	10.604 ± 0.002	11.499 ± 0.002	Vega mag
Gaia DR2 BP	11.174 ± 0.002	11.985 ± 0.002	11.843 ± 0.002	11.170 ± 0.002	12.050 ± 0.002	Vega mag
Gaia DR2 RP	9.878 ± 0.002	10.796 ± 0.002	10.742 ± 0.002	9.917 ± 0.002	10.814 ± 0.002	Vega mag
SkyMapper u	13.440 ± 0.011	14.007 ± 0.007	13.524 ± 0.011	13.376 ± 0.007	14.235 ± 0.005	AB mag
SkyMapper v	12.753 ± 0.007	13.420 ± 0.018	13.123 ± 0.011	12.790 ± 0.009	13.598 ± 0.005	AB mag
SkyMapper g	11.168 ± 0.018	11.953 ± 0.008	11.792 ± 0.007	11.146 ± 0.011	12.011 ± 0.006	AB mag
SkyMapper r	10.614 ± 0.007	11.472 ± 0.007	11.366 ± 0.007	10.627 ± 0.011	11.509 ± 0.006	AB mag
SkyMapper i	10.227 ± 0.011	11.123 ± 0.007	11.074 ± 0.005	10.241 ± 0.011	11.137 ± 0.006	AB mag
SkyMapper z	...	10.995 ± 0.007	10.963 ± 0.006	10.105 ± 0.011	10.991 ± 0.006	AB mag
2MASS J	8.969 ± 0.020	9.936 ± 0.022	9.934 ± 0.023	9.047 ± 0.026	9.945 ± 0.024	Vega mag
2MASS H	8.366 ± 0.026	9.423 ± 0.029	9.510 ± 0.023	8.509 ± 0.047	9.409 ± 0.026	Vega mag
2MASS K	8.314 ± 0.024	9.305 ± 0.019	9.384 ± 0.023	8.324 ± 0.033	9.269 ± 0.024	Vega mag
WISE W1	8.200 ± 0.022	9.228 ± 0.023	9.313 ± 0.022	8.261 ± 0.023	9.191 ± 0.023	Vega mag
WISE W2	8.222 ± 0.020	9.268 ± 0.021	9.350 ± 0.021	8.303 ± 0.020	9.226 ± 0.019	Vega mag
Stellar Properties						
Distance d_{iso}	$3.1^{+0.1}_{-0.1}$	$2.9^{+0.1}_{-0.1}$	$0.6^{+0.1}_{-0.1}$	$2.6^{+0.1}_{-0.1}$	$3.8^{+0.1}_{-0.1}$	kpc
Mass M_{\odot}	$0.78^{+0.01}_{-0.01}$	$0.79^{+0.02}_{-0.01}$	$0.86^{+0.02}_{-0.02}$	$0.85^{+0.03}_{-0.04}$	$1.42^{+0.04}_{-0.07}$	M_{\odot}
Extinction A_V	$0.095^{+0.005}_{-0.004}$	$0.013^{+0.011}_{-0.008}$	$0.131^{+0.019}_{-0.017}$	$0.006^{+0.008}_{-0.005}$	$0.148^{+0.008}_{-0.011}$	mag
Effective temperature T_{eff}	4599 ± 100	4686 ± 100	4958 ± 100	4574 ± 100	4708 ± 100	K
Surface gravity $\log g$	1.18 ± 0.15	1.69 ± 0.15	3.07 ± 0.15	1.42 ± 0.15	1.69 ± 0.15	cm s^{-2}

Table 3 continued

Table 3 (continued)

Metallicity [Fe/H]	-2.17 ± 0.13	-1.60 ± 0.15	-1.13 ± 0.28	-1.67 ± 0.14	-1.29 ± 0.19
Microturbulence ξ	1.86 ± 0.10	1.74 ± 0.10	1.43 ± 0.10	1.80 ± 0.10	1.74 ± 0.10
Orbital Properties					
Radial Velocity RV	194.2 ± 0.6	-33.5 ± 0.7	-219.7 ± 0.6	-38.2 ± 0.4	11.2 ± 0.7
Total Galactic velocity v	$296.8^{+1.7}_{-1.0}$	$372.5^{+7.3}_{-0.1}$	$431.5^{+2.9}_{-0.1}$	$387.4^{+11.7}_{-1.7}$	$274.2^{+0.9}_{-0.9}$
Pericenter R _{peri}	$5.07^{+0.05}_{-0.02}$	$6.69^{+0.01}_{-0.01}$	$7.93^{+0.01}_{-1.92}$	$7.05^{+0.08}_{-5.43}$	$5.40^{+0.81}_{-1.40}$
Apocenter R _{apo}	$11.81^{+0.18}_{-0.29}$	$25.66^{+1.18}_{-3.20}$	$62.55^{+1.39}_{-2.15}$	$35.21^{+2.89}_{-3.41}$	$15.20^{+0.05}_{-0.06}$
Eccentricity e	$0.40^{+0.01}_{-0.14}$	$0.59^{+0.01}_{-0.66}$	$0.78^{+0.04}_{-0.50}$	$0.69^{+0.20}_{-0.54}$	$0.48^{+0.11}_{-0.27}$
Maximum distance from Galactic plane z_{\max}	$10.01^{+0.14}_{-0.23}$	$10.96^{+0.53}_{-0.54}$	$18.16^{+0.50}_{-0.97}$	$10.51^{+1.10}_{-0.89}$	$5.13^{+0.27}_{-0.51}$
Total orbital energy E_{tot}	-44625^{+215}_{-268}	-15410^{+1576}_{-2767}	14360^{+608}_{-1244}	-6840^{+2769}_{-4433}	-40268^{+419}_{-242}
Angular momentum L_Z	787^{+2}_{-4}	2126^{+21}_{-40}	125^{+7}_{-9}	70^{+23}_{-38}	1005^{+8}_{-4}

^a We report random uncertainties derived under the unlikely assumption that the MIST isochrone grid perfectly reproduces all stellar properties. There are almost certainly larger systematic uncertainties that we have not investigated, though the excellent agreement between our analysis and previous results of star HE1523-0901 seems to indicate that any systematic uncertainties in our analysis cannot be too large.

^b External IDs “ESX” are stars identified in Hattori et al. (2018a).

^c Stars more likely to be of extragalactic origin.

Table 4. Chemical Abundances

Species	n	log(ϵ_X)	[X/Fe]	$\sigma_{[X/Fe]}$	n	log(ϵ_X)	[X/Fe]	$\sigma_{[X/Fe]}$	n	log(ϵ_X)	[X/Fe]	$\sigma_{[X/Fe]}$	n	log(ϵ_X)	[X/Fe]	$\sigma_{[X/Fe]}$	
Gaia EDR3 2853089398265954432																	
Na I	2	4.684	-0.179	0.150	2	2.991	-0.864	0.185	2	4.922	-0.365	0.135	2	4.082	-0.165	0.095	
Na _I NLTE	6	4.727	-0.136	...	2	2	4.805	-0.482	...	2	3.430	-0.817	...	
Mg I	2	6.252	0.059	0.074	5	5.100	-0.085	0.246	2	5.864	-0.007	0.030	7	6.582	-0.035	0.089	
Al I	1	3.674	-1.399	0.068	0.227	
Gaia EDR3 330414789019026944																	
Al _I NLTE	1	3.530	-1.543
Si I	4	6.816	0.663	0.245
K I	1	3.538	-0.175	...	1	3.401	0.696	...	1	5.200	1.063	...	1	3.007	-0.090	...	
K _I NLTE	16	5.410	0.467	0.156	16	4.270	0.335	0.068	12	4.843	0.222	0.157	23	5.519	0.152	0.067	
Ca I	4	2.126	0.343	0.288	1	0.589	-0.186	0.014	4	2.038	-0.169	0.125	
Sc II	25	3.826	0.213	0.136	8	2.920	0.315	0.129	8	3.362	0.071	0.130	34	4.042	0.005	0.061	
Ti I	22	3.956	0.343	0.201	22	2.699	0.094	0.107	27	3.032	-0.259	0.112	48	4.246	0.209	0.095	
Ti II	11	4.425	0.162	0.225	6	3.094	-0.161	0.201	4	3.948	0.007	0.163	14	4.399	-0.288	0.092	
Cr I	3	4.495	0.232	0.277	2	3.183	-0.072	0.027	3	3.357	-0.584	0.164	4	4.850	0.163	0.056	
Cr II	1	3.517	-0.546	0.002	5	3.844	-0.643	0.093	3	
Mn I	51	6.026	52	5.121	26	5.865	70	6.534	
Fe I	17	6.331	8	4.923	6	5.415	26	6.507	
Fe II	2	4.058	0.475	0.133	1	3.791	0.530	0.010	3	4.077	0.070	0.096	
Co I	11	4.737	-0.106	0.131	11	3.961	0.126	0.118	3	4.176	-0.345	0.077	24	4.932	-0.335	0.045	
Ni I	10
Cu I	1	3.043	-0.160	0.114	4
Zn I
Sr I
Sr II	2	-0.018	-0.483	0.314	1	1.887	-0.010	0.077	
Y II	5	2.201	1.348	0.200	1	-0.413	-0.258	0.011	1	0.708	0.177	0.072	5	1.059	-0.218	0.194	
Ba II	4	2.196	1.283	0.161	3	-0.822	-0.727	0.049	2	0.558	-0.033	0.136	4	1.667	0.330	0.136	
La II
Eu II	1	-0.918	-0.081	0.300	2	-1.012	0.833	0.300	3	-0.504	0.655	0.300	5	-0.213	0.200	0.300	
Gaia EDR3 3252546886080448384																	
Na I	2	4.406	0.229	0.092	2	4.245	-0.275	0.015	2	4.801	-0.356	0.075	2	3.978	-0.020	0.254	
Na _I NLTE	6	5.699	0.192	0.077	6	6.195	0.345	0.044	4	6.586	0.099	0.140	6	5.541	0.213	0.071	
Mg I	2	3.327	-1.060	0.448	1	3.365	-0.843	0.034	
Al I	2	3.888	-0.499	1	3.260	-0.948	...	
Al _I NLTE	1	5.392	-0.075	0.018	6	6.137	0.327	0.073	8	6.679	0.232	0.106	3	5.573	0.285	0.121	
Si I	1	3.230	0.203	...	1	3.510	0.140	...	1	3.969	-0.038	...	1	3.095	0.247	...	
K I	22	4.668	0.411	0.018	22	4.863	0.263	0.074	22	5.294	0.057	0.053	22	4.209	0.131	0.034	
Ca I	2	1.121	0.024	0.036	3	1.687	0.247	0.084	3	2.251	0.174	0.106	5	0.776	-0.142	0.059	
Sc II	16	3.056	0.129	0.032	36	3.324	0.054	0.060	47	3.873	-0.034	0.065	43	2.737	-0.011	0.037	
Ti I	34	3.213	0.286	0.030	49	3.641	0.371	0.080	50	4.418	0.511	0.113	58	2.927	0.179	0.036	
Ti II	8	3.348	-0.229	0.029	15	3.646	-0.274	0.055	15	4.523	-0.034	0.123	16	3.092	-0.306	0.034	
Cr I	2	2.779	0.202	0.015	3	4.167	0.247	0.214	3	4.543	-0.014	0.110	4	3.193	-0.205	0.033	
Cr II	1	2.874	-0.503	0.007	4	3.073	-0.647	0.115	5	3.565	-0.792	0.072	2	2.827	-0.371	0.293	
Mn I	42	5.361	59	5.720	49	6.325	74	5.272	
Fe I	16	5.560	17	5.902	16	6.612	24	5.134	
Fe II
Co I	9	4.014	-0.143	0.036	22	2.962	-0.278	0.107	5	3.816	-0.061	0.059	1	2.541	-0.177	0.010	
Ni I	22	4.334	-0.166	0.043	26	4.966	-0.171	0.109	26	3.811	-0.167	0.037	
Cu I	1	1.856	-0.624	0.010	1	3.001	-0.116	0.034	11
Zn I	1	2.224	-0.293	0.008	1	2.938	0.078	0.037	1	3.504	0.007	0.068	2	2.241	-0.097	0.008	
Gaia EDR3 631782858097175936																	
Na I	2	4.082	-0.165	0.095	2	3.430	-0.817	...	2	3.885	-0.113	...	2	3.342	-0.435	...	
Mg I	4	5.642	0.065	0.227	4
Al I
Al _I NLTE	1	2.832	-1.155	0.043
Si I	3	5.099	0.032	0.201
K I	15	4.094	0.237	0.175
Ca I	5	0.454	-0.243	0.065
Sc II	28	2.841	0.314	0.131
Ti I	46	2.800	0.273	0.068
Ti II	15	2.844	-0.333	0.063
Cr I	3	2.882	-0.295	0.092
Cr II	61	5.083
Mn I	20	4.814
Fe I
Fe II
Co I
Ni I
Cu I
Zn I

Table 4 continued

Table 4 (continued)

Species	n	log(ϵ_X)	[X/Fe]	σ [X/Fe]	n	log(ϵ_X)	[X/Fe]	σ [X/Fe]	n	log(ϵ_X)	[X/Fe]	σ [X/Fe]	n	log(ϵ_X)	[X/Fe]	σ [X/Fe]	
Sr I
Sr II	2	0.819	0.032	0.152	...	1	0.944	-0.186	0.013	1	1.133	-0.634	0.032	1	0.227	-0.381	0.006
Y II	2	1.240	0.110	0.071	2	1.764	-0.003	0.113	2	0.442	-0.166	0.098	
Ba II	1	0.342	0.115	0.038	2	0.557	0.047	0.104	3	1.182	0.035	0.324	3	-0.399	-0.387	0.027	
La II	2	0.781	0.211	0.113	2	1.519	0.312	0.145	4	-0.089	-0.137	0.100	
Eu II	3	-1.262	0.261	0.200	4	-0.904	0.276	0.200	5	-0.411	0.132	0.200	4	-1.210	0.492	0.300	
Gaia EDR3 6479574961975897856																	
Na I
Na I _{NLTE}	2	4.011	-0.480	0.130	2	4.912	0.066	0.060	2	4.393	-0.073	0.020	
Mg I	7	5.751	0.499	0.078	8	5.929	0.108	0.042	5	6.322	0.146	0.079	5	6.184	0.388	0.070	
Al I	1	3.387	-0.745	0.115	1	3.583	-1.118	0.002	
Al I _{NLTE}	1	3.231	-0.901	...	1	3.405	-1.296	
Si I	7	5.774	0.562	0.049	6	6.028	0.247	0.041	8	6.573	0.437	0.090	7	6.071	0.315	0.087	
K I _{NLTE}	1	1	3.536	0.195	...	1	3.697	0.001	...	1	3.648	0.332	...	
Ca I	21	4.346	0.344	0.096	23	4.773	0.202	0.061	22	5.193	0.267	0.039	22	4.922	0.376	0.073	
Sc II	5	0.989	0.147	0.092	5	1.443	0.032	0.076	5	2.104	0.338	0.121	3	1.547	0.161	0.089	
Ti I	54	2.879	0.207	0.091	58	3.232	-0.009	0.047	46	3.655	0.059	0.031	51	3.416	0.200	0.069	
Ti II	59	3.140	0.468	0.054	61	3.575	0.334	0.057	46	3.977	0.381	0.104	52	3.601	0.385	0.086	
Cr I	15	3.013	-0.309	0.125	17	3.569	-0.322	0.040	14	4.084	-0.162	0.040	15	3.713	-0.153	0.077	
Cr II	4	3.460	0.138	0.064	5	4.057	0.166	0.088	4	4.474	0.228	0.114	3	3.968	0.102	0.052	
Mn I	6	2.768	-0.354	0.077	6	3.078	-0.613	0.054	5	3.685	-0.361	0.033	6	3.176	-0.490	0.037	
Fe I	48	5.109	72	5.686	63	6.000	65	5.675	
Fe II	20	5.293	25	5.860	22	6.325	23	5.793	
Co I	3	2.746	0.104	0.112	2	3.178	-0.033	0.146	1	3.622	0.056	0.026	2	2.987	-0.199	0.160	
Ni I	26	3.843	-0.059	0.073	31	4.191	-0.280	0.069	27	4.738	-0.088	0.056	28	4.318	-0.128	0.033	
Cu I	1	1.594	-0.857	0.005	1	2.472	-0.334	0.030	1	1.921	-0.505	0.014	
Zn I	2	2.459	0.197	0.039	2	2.832	0.001	0.043	2	3.370	0.184	0.081	1	2.794	-0.012	0.044	
Sr I	1	0.429	-0.103	0.013	1	0.685	-0.416	0.011	1	1.215	-0.241	0.011	1	0.862	-0.214	0.014	
Sr II	2	0.683	0.151	0.092	2	0.999	-0.102	0.108	2	1.520	0.064	0.180	2	1.158	0.082	0.102	
Y II	4	-0.253	-0.165	0.103	5	0.261	-0.220	0.053	4	0.958	0.122	0.136	5	0.438	-0.018	0.076	
Ba II	3	0.095	0.123	0.098	4	0.585	0.044	0.110	2	1.280	0.384	0.142	2	0.565	0.049	0.144	
La II	2	-0.830	0.358	0.029	3	-0.402	0.217	0.072	1	0.366	0.630	0.097	2	-0.327	0.317	0.040	
Eu II	4	-1.472	0.305	0.300	4	-1.028	0.180	0.300	3	-0.588	0.266	0.300	5	-0.900	0.334	0.200	
Gaia EDR3 6558932694746826240																	
Na I
Na I _{NLTE}	2	4.011	-0.480	0.130	2	4.912	0.066	0.060	2	4.393	-0.073	0.020	
Mg I	7	5.751	0.499	0.078	8	5.929	0.108	0.042	5	6.322	0.146	0.079	5	6.184	0.388	0.070	
Al I	1	3.387	-0.745	0.115	1	3.583	-1.118	0.002	
Al I _{NLTE}	1	3.231	-0.901	...	1	3.405	-1.296	
Si I	7	5.774	0.562	0.049	6	6.028	0.247	0.041	8	6.573	0.437	0.090	7	6.071	0.315	0.087	
K I _{NLTE}	1	1	3.536	0.195	...	1	3.697	0.001	...	1	3.648	0.332	...	
Ca I	21	4.346	0.344	0.096	23	4.773	0.202	0.061	22	5.193	0.267	0.039	22	4.922	0.376	0.073	
Sc II	5	0.989	0.147	0.092	5	1.443	0.032	0.076	5	2.104	0.338	0.121	3	1.547	0.161	0.089	
Ti I	54	2.879	0.207	0.091	58	3.232	-0.009	0.047	46	3.655	0.059	0.031	51	3.416	0.200	0.069	
Ti II	59	3.140	0.468	0.054	61	3.575	0.334	0.057	46	3.977	0.381	0.104	52	3.601	0.385	0.086	
Cr I	15	3.013	-0.309	0.125	17	3.569	-0.322	0.040	14	4.084	-0.162	0.040	15	3.713	-0.153	0.077	
Cr II	4	3.460	0.138	0.064	5	4.057	0.166	0.088	4	4.474	0.228	0.114	3	3.968	0.102	0.052	
Mn I	6	2.768	-0.354	0.077	6	3.078	-0.613	0.054	5	3.685	-0.361	0.033	6	3.176	-0.490	0.037	
Fe I	48	5.109	72	5.686	63	6.000	65	5.675	
Fe II	20	5.293	25	5.860	22	6.325	23	5.793	
Co I	3	2.746	0.104	0.112	2	3.178	-0.033	0.146	1	3.622	0.056	0.026	2	2.987	-0.199	0.160	
Ni I	26	3.843	-0.059	0.073	31	4.191	-0.280	0.069	27	4.738	-0.088	0.056	28	4.318	-0.128	0.033	
Cu I	1	1.594	-0.857	0.005	1	2.472	-0.334	0.030	1	1.921	-0.505	0.014	
Zn I	2	2.459	0.197	0.039	2	2.832	0.001	0.043	2	3.370	0.184	0.081	1	2.794	-0.012	0.044	
Sr I	1	0.429	-0.103	0.013	1	0.685	-0.416	0.011	1	1.215	-0.241	0.011	1	0.862	-0.214	0.014	
Sr II	2	0.683	0.151	0.092	2	0.999	-0.102	0.108	2	1.520	0.064	0.180	2	1.158	0.082	0.102	
Y II	4	-0.253	-0.165	0.103	5	0.261	-0.220	0.053	4	0.958	0.122	0.136	5	0.438	-0.018	0.076	
Ba II	3	0.095	0.123	0.098	4	0.585	0.044	0.110	2	1.280	0.384	0.142	2	0.565	0.049	0.144	
La II	2	-0.830	0.358	0.029	3	-0.402	0.217	0.072	1	0.366	0.630	0.097	2	-0.327	0.317	0.040	
Eu II	4	-1.472	0.305	0.300	4	-1.028	0.180	0.300	3	-0.588	0.266	0.300	5	-0.900	0.334	0.200	
Gaia EDR3 655619232329517108352																	
Na I
Na I _{NLTE}	2	4.011	-0.480	0.130	2	4.912	0.066	0.060	2	4.393	-0.073	0.020	
Mg I	7	5.751	0.499	0.078	8	5.929	0.108	0.042	5	6.322	0.146	0.079	5	6.184	0.388	0.070	
Al I	1	3.387	-0.745	0.115	1	3.583	-1.118	0.002	
Al I _{NLTE}	1	3.231	-0.901	...	1	3.405	-1.296	
Si I	7	5.774	0.562	0.049	6	6.028	0.247	0.041	8	6.573	0.437	0.090	7	6.071	0.315	0.087	
K I _{NLTE}	1	1	3.536	0.195	...	1	3.697	0.001	...	1	3.648	0.332	...	
Ca I	21	4.346	0.344	0.096	23	4.773	0.202	0.061	22	5.193	0.267	0.039	22	4.922	0.376	0.073	
Sc II	5	0.989	0.147	0.092	5	1.443	0.032	0.076	5	2.104	0.338	0.121	3	1.547	0.161	0.089	
Ti I	54	2.879	0.207	0.091	58	3.232	-0.009	0.047	46	3.655	0.059	0.031	51	3.416	0.200	0.069	
Ti II	59	3.140	0.468	0.054	61	3.575	0.334	0.057	46	3.977	0.381	0.104	52	3.601	0.385	0.086	
Cr I	15	3.013	-0.309	0.125	17	3.569	-0.322	0.040	14	4.084	-0.162	0.040	15	3.713	-0.153	0.077	
Cr II	4	3.460	0.138	0.064	5	4.057	0.166	0.088	4	4.474	0.228	0.114	3	3.968	0.102	0.052	
Mn I	6	2.768	-0.354	0.077	6	3.078	-0.613	0.054	5	3.685	-0.361	0.033	6	3.176	-0.490	0.037	
Fe I	48	5.109	72	5.686	63	6.000	65	5.675	
Fe II	20	5.293	25	5.860	22	6.325	23	5.793	
Co I	3	2.746	0.104	0.112	2	3.178	-0.033	0.146	1	3.622	0.056	0.026	2	2.987	-0.199	0.160	
Ni I	26	3.843	-0.059	0.073	31	4.191	-0.280	0.069	27	4.738	-0.088	0.056	28	4.318	-0.128	0.033	
Cu I	1	1.594	-0.857	0.005	1	2.472	-0.334	0.030	1	1.921	-0.505	0.014	
Zn I	2	2.459	0.197	0.039	2	2.832	0.001	0.043	2	3.370	0.184	0.081	1	2.794	-0.012	0.044	
Sr I	1	0.429	-0.103	0.013	1	0.685	-0.416	0.011	1	1.215	-0.241	0.011	1	0.862	-0.214	0.014	
Sr II	2	0.683	0.151	0.092	2	0.999	-0.102	0.108	2	1.520	0.064	0.180	2	1.158	0.082	0.102	
Y II	4	-0.253	-0.165	0.103	5	0.261	-0.220	0.053	4	0.958	0.122	0.136	5	0.438	-0.018	0.076	
Ba II	3	0.095	0.123	0.098</													